Astronomy & Astrophysics manuscript no. folini-walder June 27, 2006
(DOI: will be inserted by hand later)

Supersonic turbulence in shock-bound interaction zones I: symmetric settings

Doris Folini[1] and Rolf Walder[2,3]

[1] Institut für Astronomie, ETH Zürich, CH-8092 Zürich, Switzerland; E-mail: folini@astro.phys.ethz.ch,
[2] Observatoire de Strasbourg, 67000 Strasbourg, France; E-mail: walder@astro.phys.ethz.ch
[3] Max-Planck-Institut für Astrophysik, 85741 Garching, Germany;

Received ... ; accepted ...

Abstract. Colliding hypersonic flows play a decisive role in many astrophysical objects. They contribute, for example, to molecular cloud structure, the X-ray emission of O-stars, differentiation of galactic sheets, the appearance of wind-driven structures, or, possibly, the prompt emission of γ-ray bursts. Our intention is the thorough investigation of the turbulent interaction zone of such flows, the cold dense layer (CDL). In this paper, we focus on the idealized model of a 2D plane parallel isothermal slab and on symmetric settings, where both flows have equal parameters. We performed a set of high-resolution simulations with upwind Mach numbers, $5 < M_{\rm u} < 90$. We find that the CDL is irregularly shaped and has a patchy and filamentary interior. The size of these structures increases with $\ell_{\rm cdl}$, the extension of the CDL. On average, but not at each moment, the solution is about self-similar and depends only on $M_{\rm u}$. We give the corresponding analytical expressions, with numerical constants derived from the simulation results. In particular, we find the root mean square Mach number to scale as $M_{\rm rms} \approx 0.2 M_{\rm u}$. Independent of $M_{\rm u}$ is the mean density, $\rho_{\rm m} \approx 30\rho_{\rm u}$. The fraction $f_{\rm eff}$ of the upwind kinetic energy that survives shock passage scales as $f_{\rm eff} = 1 - M_{\rm rms}^{-0.6}$. This dependence persists if the upwind flow parameters differ from one side to the other of the CDL, indicating that the turbulence within the CDL and its driving are mutually coupled. In the same direction points the finding that the auto-correlation length of the confining shocks and the characteristic length scale of the turbulence within the CDL are proportional.
In summary, larger upstream Mach numbers lead to a faster expanding CDL with more strongly inclined confining interfaces relative to the upstream flows, more efficient driving, and finer interior structure relative to the extension of the CDL.

Key words. Shock waves – Instabilities – Turbulence – Hydrodynamics – ISM:kinematics and dynamics – Stars:winds, outflows

1. Introduction

Supersonically turbulent, shock-bound interaction zones are important for a variety of astrophysical objects. They contribute, for example, to structure formation in molecular clouds (Hunter et al. 1986; Ballesteros-Paredes et al. 1999a; Hartmann et al. 2001; Hueckstaedt 2003; Heyer & Brunt 2004; Vázquez-Semadeni 2004) and galaxy formation (Anninos & Norman 1996; Kang et al. 2005). They affect the X-ray emission of line-driven hot star winds (Owocki et al. 1988; Feldmeier et al. 1997; Feldmeier & Owocki 1998; Oskinova et al. 2004) and contribute substantially to the physics and emitted spectrum of colliding wind binaries (Stevens et al. 1992; Nussbaumer & Walder 1993; Folini & Walder 2000; Marchenko et al. 2003; Corcoran et al. 2005). The currently most promising model for the prompt emission of γ-ray bursts is based on internal shocks (Rees & Meszaros 1994; Panaitescu et al. 1999; Piran 2004; Fan & Wei 2004). A similar mechanism has been proposed for micro-quasars (Kaiser et al. 2000), BL Lacs and Blazars (Ghisellini et al. 2002; Mimica et al. 2004), and Herbig-Haro objects (Matzner & McKee 1999).

So far, the shape and turbulent interior of shock-bound interaction zones were mostly studied separately. In this paper we focus on the system as a whole, stressing that upwind flows, confining interfaces of the interaction zone, and interior structure of this zone form a tightly coupled system. The turbulence within the interaction zone affects the shape of the confining shocks which, in turn, determines how much energy is thermalized at these shock and how much energy remains available for driving the turbulence.

On the shape and stability of 2D interaction zones a variety of papers have been written, of which we mention only a few. Vishniac (1994) showed by analytical

Send offprint requests to: D. Folini

means that geometrically thin, isothermal, 2D, planar, shock-bounded slabs are non-linearly unstable, coining the term non-linear thin shell instability or NTSI for this instability. Blondin & Marks (1996) essentially reproduce these analytical predictions numerically, mentioning also the occurrence of supersonic turbulence within the slab. Performing 2D radiative and isothermal simulations of colliding molecular clouds Klein et al. (1998) observe complex shaping and instability of the collision zone. The role of a radiative cooling layer was addressed by several authors. Strickland & Blondin (1995) numerically investigated flows against a wall in 2D, finding that an unstable cooling layer introduces disturbances in the interface separating the cooling layer from the cooled matter. Walder & Folini (1998a), looking at colliding flows instead of a flow against a wall, show that one unstable cooling layer is sufficient to destabilize both confining interfaces of the cooled matter. In addition, the cooled matter becomes supersonically turbulent. If self-gravity is included fragmentation of the interaction zone is observed (Anninos & Norman 1996; Hunter et al. 1986).

On supersonic turbulence an overwhelming amount of literature meanwhile exists. At least part of this attention arises because it is thought that supersonic turbulence can explain the structuring and support of molecular clouds and thus plays a decisive role for star formation. A comprehensive view of this issue can be found in the recent reviews by Mac Low & Klessen (2004), Elmegreen & Scalo (2004), and Scalo & Elmegreen (2004). Of particular interest for the work we present here is the paper by Mac Low (1999), where Figure 4 shows that for monochromatically driven turbulence in a 3D periodic box the wave-length of the driving is apparent in the spatial scale of the turbulent structure. The possible importance of the finite size of the slab was recently pointed out by Burkert & Hartmann (2004).

With this paper we want to make four points. First, we argue that within the frame of isothermal Euler equations and in infinite space the solution, at least to first approximation, may be self-similar and dependent only on the upstream Mach number. Based on this assumption we give expressions for average quantities of the slab. Second, we show that the numerical solution, which is defined on a finite computational domain only and includes (implicit) numerical dissipation, remains close to self-similar as long as the width of the slab is small and the root mean square Mach number larger than one. Third, we stress the tight mutual coupling between the turbulence and its driving. Fourth, we point out that spatial scales generally grow with the extension $\ell_{\rm cdl}$ of the interaction zone, but decrease with increasing upstream Mach number $M_{\rm u}$.

The results we are going to present are based on a set of simulations which differ only in their upwind Mach numbers. In this paper we restrict the analysis of these simulations to the above mentioned three objectives. A more detailed analysis of the interior structure of the interaction zone we postpone to a subsequent paper.

In the following, we first give in Sect. 2 the details on our physical model and numerical method. In Sect. 3 we derive the self-similar scaling relations. The numerical results in we present in Sect. 4. Discussion follows in Sect. 5, conclusions come in Sect. 6.

2. Physical model and numerical method

The numerical treatment of supersonic turbulence is an issue in its own right, and we start this section with a brief summary of some results that are relevant for the present work. We then specify the physical model we consider, detail what numerical method we use, and what simulations we perform.

2.1. Simulating supersonic turbulence

The shock compressed layer we study in this paper is supersonically turbulent, with root mean square Mach numbers between about 1 and 10. An important fraction of the kinetic energy is dissipated in shocks. Euler equations are sufficient to describe this part of the problem. A cascade transfers the remaining energy to higher and higher wave numbers until it is finally destroyed at the viscous dissipation scale. To capture also this part of the problem, the compressible Navier-Stokes equations should in principle be used. However, the range of spatial scales associated with the energy cascade exceeds the capacity of any computer by far.

In subsonic turbulence, one way out is to use a suitable sub-grid scale model. The model is used to compute an effective viscosity coefficient, which should mimic as precisely as possible the cascading between the smallest scale still resolved by the numerical grid and the viscous dissipation scale. This coefficient then is used in the Navier-Stokes equations, instead of the physical viscosity (see e.g. Lesieur (1999)). For the approach to work it is essential that the effective viscosity obtained from the sub-grid scale model exceeds the (implicit) numerical viscosity of the overall numerical scheme. In subsonic turbulence this can be achieved by the use of low-dissipation schemes (see e.g. Lele (1992)).

In supersonic turbulence, explicit sub-grid scale modeling in the above sense so far does not exist. The basic reason is that the numerical treatment of supersonic turbulence requires schemes that can treat shocks appropriately, like the widely used shock capturing schemes. The (implicit) numerical viscosity of such schemes is, however, much too large to match the above requirement, even if the schemes are of high order (Garnier et al. 1999; Porter et al. 1992). A strategy for this case, the so called MILES approach (Monotone Integrated Large-Eddy Simulation), was proposed by Boris et al. (1992) and further explored by Porter et al. (1992) and Porter et al. (1994). The basic claim is that the numerical viscosity inherent to shock capturing schemes (see e.g. Hirsch (1995); LeVeque (2002)) acts already as a physically correct sub-grid scale model.

Solving the Euler equations by means of a shock capturing scheme thus should yield the correct physical answer.

The validity of this claim, that implicit numerical viscosity alone leads to a correct physical solution, was investigated by Garnier et al. (1999) for a selection of shock capturing schemes, among them a MUSCL-scheme (Monotone Upwind Scheme for Conservation Laws) similar to the one we use (see Sect. 2.3). For the cases considered (essentially decaying subsonic), they found that the scheme indeed acts as a (very dissipative) sub-grid scale model in that it preserves the flow from energy accumulation at small spatial scales. However, they also found that structures defined on less than 5 grid points are affected by substantial numerical damping. Porter et al. (1994) found, in addition, that the dissipation properties of their scheme (MUSCL with PPM) are highly non-linear and also not only depend on the grid spacing but also on the wavelength of the flow structure. Structures on less than 32 grid points are affected by numerical damping.

We rely on the MILES approach in this paper. This in lack of a better model and although, to our knowledge, the validity and quality of the approach was never tested for supersonic turbulence. The numerical solutions we obtain thus are rather solutions of the Navier-Stokes equations. Nevertheless, as dissipation in shocks dominates by far over numerical dissipation, we expect the 'Euler character' of the solution to prevail.

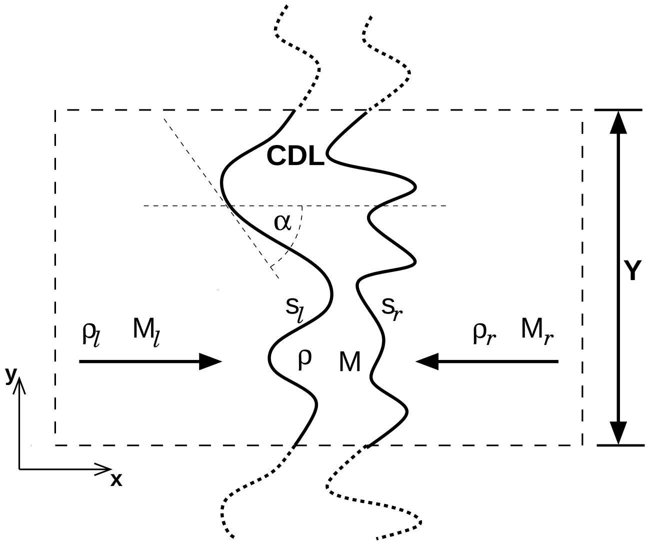

Fig. 1. Sketch of physical model problem. $\rho_{\rm i}$, $M_{\rm i}$, and $s_{\rm i}$ denote the density, Mach number, and confining shock of the left $(i = l)$ and right $(i = r)$ flow. ρ and M denote the density and Mach number of the CDL. α is the absolute value of the angle between the x-axis and the tangent to the shock. CDL is the shock compressed interaction zone. The dashed rectangle indicates the computational domain with y-extension Y. Periodic boundary conditions in y-direction imply periodic continuation of the solution (dotted continuation of left and right shock).

2.2. The model problem

The model problem we consider consists of a 2D, plane parallel, infinitely extended, isothermal, shock compressed slab. A sketch is given in Fig. 1. Two high Mach number flows, oriented parallel (left flow, subscript l) and anti-parallel (right flow, subscript r) to the x-direction, collide head on. The resulting high density interaction zone, the shock compressed slab, is oriented in y-direction. We denote this interaction zone by CDL for 'cold dense layer', to remain consistent with notation used already in Walder & Folini (1996a) and Walder & Folini (1998a). We investigate this system within the frame of Euler equations (but see also Sect. 2.1), together with a polytropic equation of state,

$$\frac{\partial \rho}{\partial t} + \boldsymbol{\nabla}\left(\rho \boldsymbol{v}\right) \;=\; 0, \tag{1}$$

$$\frac{\partial \rho \boldsymbol{v}}{\partial t} + \boldsymbol{\nabla}\left(\rho \boldsymbol{v} \otimes \boldsymbol{v} + \frac{p}{\mu} I\right) \;=\; 0, \tag{2}$$

$$\frac{\partial E}{\partial t} + \boldsymbol{\nabla}(\boldsymbol{v}\left(E + p\right)) \;=\; 0, \tag{3}$$

$$e \;=\; p/(\gamma - 1). \tag{4}$$

Here, ρ is the particle density, μ the average mass per particle, $\boldsymbol{v} = (v_{\rm x}, v_{\rm y})$ is the velocity vector, p is thermal pressure, e the thermal energy density, and $E = \rho \boldsymbol{v}^2/2 + e$ the total energy density. I is the identity tensor. For the polytropic exponent we choose $\gamma = 1.000001$. This value guarantees that jump conditions and wave speeds of a Mach 90 shock are within 0.01 per cent of the isothermal values.

Within the frame of this paper we consider symmetric settings only, where the left (subscript l) and right (subscript r) colliding flow have identical parameters (subscript u for upstream): $\rho_{\rm l} = \rho_{\rm r} \equiv \rho_{\rm u}$ and $|v_{\rm l}| = |v_{\rm r}| \equiv v_{\rm u}$.

We look at the problem in dimensionless form. Velocities we express in units of the isothermal sound speed $a = \sqrt{T k_{\rm B}/\mu}$, with T the temperature and $k_{\rm B}$ the Boltzmann constant. Densities we express in terms of the upstream density $\rho_{\rm u}$. Finally, we express lengths in units of Y_0, the smallest y-extent of the computational domain we have used. This artificial choice is necessary as there is no natural time independent length scale to the problem (see Sect. 3).

2.3. Numerical method

Our results are computed with the AMRCART-code[1]. We used the multidimensional high-resolution finite volume integration scheme developed by Colella (1990) on the basis of a Cartesian mesh. Tests show that this algorithm, compared to dimensional splitting schemes, is significantly more accurate in capturing flow features not aligned with

[1] AMRCART is part of the A-MAZE code-package (Walder & Folini 2000a), which contains 3D adaptive MHD and radiative transfer codes. The package, along with a brief description, is publicly available at
http://www.astro.phys.ethz.ch/staff/folini/folini.html or
http://www.astro.phys.ethz.ch/staff/walder/walder.html.

the axis of the mesh. In all our simulations we used a version of the scheme which is (formally) second order accurate in space and in time for smooth flows.

This integration scheme we combined with the adaptive mesh algorithm by Berger (1985). While for the upwind flows a rather coarse mesh is sufficient, the turbulent CDL is resolved on a much finer scale.

We found it useful to have our CDL moving in positive x-direction at a speed of about Mach 20-40. If the CDL is essentially stationary with respect to the computational grid, we observed alignment effects of strong shocks which are nearly parallel to a cell interface (in y-direction). Through the global motion of the CDL, which implies supersonic motion of the confining shocks with respect to the computational grid, we got rid of this problem. We have checked that this procedure introduces no systematic effects into the solution. The problem of alignment effects when dealing with high Mach number flows, nearly stationary shocks, and high order upwind schemes is well known and not particular to our scheme (Colella & Woodward 1984; Quirk 1994; Jasak & Weller 1995). Other work arounds exist, as for example smoothing of interfaces by additional viscosity, which is often applied in PPM implementations.

2.3.1. Numerical settings and integration time

In x-direction, our computational domain extends over $200\,\mathrm{Y}_0$. The y-extent Y of our domain varies between simulations, $\mathrm{Y}_0 \leq \mathrm{Y} \leq 6\,\mathrm{Y}_0$ (see Table B.1). Boundary conditions at the left and right boundary (x-direction) are 'supersonic inflow'. In y-direction we have periodic boundary conditions. The cell size on the coarsest level is $0.2\,\mathrm{Y}_0$. The cells on the finest level, covering the CDL, are smaller by a factor 2^6 to 2^9, yielding between 320 and 2560 cells over a distance Y_0 (depending on the simulation, see Table B.1).

As will be shown, the relevant time dependent quantity for the evolution of CDL mean quantities is the average x-extension of the CDL, $\ell_{\rm cdl}$. We define it as $\ell_{\rm cdl} \equiv V/\mathrm{Y}$, where V is the 2D volume of the CDL. For later use we also introduce the volume integrated density $m_{\rm cdl} \equiv \int_{\rm V} \rho$, the mean density $\rho_{\rm m} \equiv m_{\rm cdl}/V$, and the average column density $N \equiv m_{\rm cdl}/\mathrm{Y} = \rho_{\rm m}\ell_{\rm cdl}$. The last quantity is made dimensionless by division through $N_0 \equiv \rho_{\rm u}\mathrm{Y}_0$. Most simulations we stopped at $\ell_{\rm cdl} = \mathrm{Y}/2$.

2.3.2. Initial conditions

We investigate three different initial conditions, I=0,1,2.

I=0: No CDL exists at $t = 0$. The left and right flow are initially separated by a single interface. The interface is wiggled with a single, sinusoidal mode of wave-length $0.1\,\mathrm{Y}$ and amplitude $0.0195\,\mathrm{Y}_0$ (about 3 to 25 grid cells, depending on the discretization).

I=1: A CDL is present at time $t = 0$. It has a column density of $N = 14\,N_0$ and a thickness of $0.03125\,\mathrm{Y}_0$. The confining shocks are both wiggled, with the same sinusoidal mode and amplitude as the interface in the case I=0. The mass within the CDL is at rest and of constant density, $\rho = \rho_{\rm u} M_{\rm u}^2$, the density the CDL would have in 1D. Note that this initialization implies some violation of the Rankine-Hugoniot jump conditions at the interfaces.

I=2: A CDL is present at time $t = 0$, with column density $N = 56\,N_0$ and a thickness of $0.125\,\mathrm{Y}_0$. The right shock is wiggled as for I=1, the left shock is straight. The density and velocity in the CDL are set as for I=1.

We stress that the initial wiggling of the shocks is not compelling. The only effect of this wiggling is to speed up the initial phase of the evolution. Test cases using another wiggling or starting from straight shocks end up similarly as the simulations we are going to present in the following.

We would like to add a side note on this last point, on our observation that the slab is destabilized also when bound by straight shocks. This was already reported by Blondin & Marks (1996), who ascribed the destabilization to 'numerical noise'. Meanwhile, Robinet et al. (2000) have investigated in some more detail what is called the carbuncle phenomenon. They showed that - contrary to what was believed so far - a single straight shock is linearly unstable for exactly one mode associated to the upstream Mach number of $M_{\rm crit} = [(5+\gamma)/(3-\gamma)]^{1/2}$. For isothermal conditions this yields $M_{\rm crit} = \sqrt{3}$. They also showed that this single unstable mode is sufficient to make straight shocks aligned with the mesh numerically unstable at all Mach numbers if the computation is done with a low viscosity high order shock capturing scheme. To what degree this instability for a straight shock of any Mach number is really physical seems an open question to us.

2.4. *The different runs*

The runs we performed are listed in Table B.1. They differ in their upwind Mach numbers, which lie in a range $5 \lesssim M_{\rm u} \lesssim 90$, as well as in their initialization, numerical discretization, and y-extent of the domain. The labels of the different runs are built up as M_I.R.Y. Here, M is the upwind Mach number. I is the initialization (0,1, or 2). R gives the refinement of the spatial discretization, relative to the coarsest grid simulation we performed (1, 2, 4, or 8). R=1 corresponds to a finest cell size of about $3 \cdot 10^{-3}\,\mathrm{Y}_0$, R=2 indicates a two times smaller cell size. Y is the domain size (1, 2, 4, or 6) in units of Y_0. For example, R22_0.2.4 denotes a run with $M_{\rm u} = 22$, initialization I=0, finest cell size about $1.5 \cdot 10^{-3}\mathrm{Y}_0$, and y-extent $4\,\mathrm{Y}_0$.

3. Scaling properties of model problem

Within the frame of Euler equations and in infinite space, the problem of isothermal supersonically colliding flows can be solved analytically in 1D. The solution, sketched in Fig. 2 and Sect. 3.1, is self-similar and depends only on two free parameters, the Mach numbers of the left and right upwind flow.

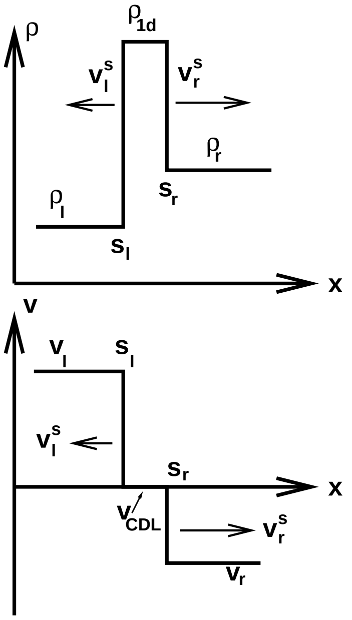

Fig. 2. The self-similar 1D solution of isothermal colliding supersonic flows in density (top) and velocity (bottom). The interaction zone (labeled CDL) is bounded by two shocks, s_l and s_r, having speeds v_l^s and v_r^s in the rest frame of the CDL. The density and velocity of the 1D interaction zone we denote by $\rho_{1\mathrm{d}}$ and $v_{1\mathrm{d}}$ respectively.

In 2D the situation is more complicated. The solution is unstable (Vishniac 1994; Blondin & Marks 1996), the shocks confining the CDL are non-stationary and oblique, the interior of the CDL is supersonically turbulent.

Nevertheless, in infinite space it seems reasonable to *assume* that the solution, on average, may still evolve in a self-similar manner. We base this assumption on the following two observations. First, the isothermal Euler equations are scale free in infinite space. Second, the free parameters of the problem (ρ_u, M_u, and a) do not introduce any fixed length or time scale. Under these conditions, it is possible that the solution also does not depend on length or time separately, but only on their ratio. If so, all length scales should evolve equally with time, which implies, in particular, that the solution then should not depend on the extension of the CDL. We stress, however, that *we have no proof of the above assumption of self-similarity.*

In the remainder of this section, we are going to elaborate a bit further on the implications of the assumed self-similarity. In Sect. 4 we will see that the relations derived here give a good approximation to the numerical results. Three important points we stress already here. The numerical simulations are carried out in finite space (not infinite space), numerical dissipation might play a role, and the simulations are for the most part stopped while the CDL is still small, about half the size of the y-extent of the the computational domain. Important aspects that can be obtained only from the numerical solution include quantities related to the driving of the turbulence, the values of proportionality constants, and the interior structure of the CDL. This last aspect we neglect, however, in the current paper and focus on mean quantities instead.

3.1. Self-similar 1D solution

Denoting the density and velocity of the CDL by $\rho_{1\mathrm{d}}$ and $v_{1\mathrm{d}}$, and those of the left and right upwind flow by ρ_i and v_i ($i = l, r$), the solution in the rest frame of the CDL is given by

$$\rho_{1\mathrm{d}}/\rho_\mathrm{i} \;=\; M_\mathrm{i}^2 + 1 \approx M_\mathrm{i}^2, \tag{5}$$

$$v_{1\mathrm{d}} \;=\; 0, \tag{6}$$

$$|v_\mathrm{i}^s| \;=\; aM_\mathrm{i}/(M_\mathrm{i}^2 - 1) \approx a/M_\mathrm{i} << a. \tag{7}$$

Here v_i^s is the velocity of the confining shocks and a is again the isothermal sound speed. The approximations hold for large Mach numbers. The self-similar character is apparent: the solution is not a function of x and t but only, through v_i^s, a function of x/t.

A relation between characteristic length and time scales of the solution, the self-similarity variable $\kappa_{1\mathrm{d}}$, can be obtained as follows. As length scale we take the spatial extension $\ell_{1\mathrm{d}}$ of the CDL, as time scale the time τ needed to accumulate the corresponding column density $N_{1\mathrm{d}}$. From the relations

$$N_{1\mathrm{d}} = \rho_{1\mathrm{d}}\ell_{1\mathrm{d}}. \tag{8}$$

and

$$N_{1\mathrm{d}} = \tau\left(\rho_l v_l + \rho_r v_r\right) \tag{9}$$

and using $\rho_\mathrm{l}/\rho_\mathrm{r} = M_\mathrm{r}^2/M_\mathrm{l}^2$ (see Eq. 5), we obtain

$$\kappa_{1\mathrm{d}} \equiv \frac{\ell_{1\mathrm{d}}}{\tau} = a\frac{M_l + M_r}{M_l \cdot M_r}. \tag{10}$$

Thus for strong shocks $\kappa_{1\mathrm{d}}$ is nothing else than $|v_\mathrm{l}^s| + |v_\mathrm{r}^s|$. Specializing to symmetric settings ($\mathrm{l} = \mathrm{r}$) yields $\rho_{1\mathrm{d}}/\rho_\mathrm{u} = M_\mathrm{u}^2$ and $\kappa_{1\mathrm{d}} = 2a/M_\mathrm{u}$.

3.2. Scaling properties of 2D symmetric solution

In the following, we derive scaling relations for the 2D solution, assuming self-similarity. We confront these relations with corresponding numerical results in Sect. 4.

3.2.1. Density, Mach number, self-similarity variable

In the following, all velocities are again given in the rest frame of the CDL and we *assume* that a self-similar solution exists. A natural choice for the (constant) self-similarity variable then is again $\kappa_{2\mathrm{d}} \equiv \ell_\mathrm{cdl}/\tau$. Using the definitions of Sect. 2.3.1 we must have, as in the 1D case,

$$N \;=\; \rho_\mathrm{m}\ell_\mathrm{cdl}, \tag{11}$$

$$N \;=\; 2\tau\rho_\mathrm{u}v_\mathrm{u}. \tag{12}$$

Dividing the two equations through each other yields $\kappa_{2\mathrm{d}} = 2\rho_\mathrm{u}v_\mathrm{u}/\rho_\mathrm{m}$. As $\kappa_{2\mathrm{d}}$ is a constant, the CDL mean density ρ_m must be constant in time. The root mean square velocity $v_{\rm rms}^2$ then has to be constant in time as well, at least if the CDL density and velocity, ρ and v, are uncorrelated (in which case we can replace the average over the product ρv^2 by the product of the averages of ρ and v^2) and if kinetic pressure dominates over thermal pressure. This can be seen from equating the total upwind pressure with the total pressure within the CDL,

$$\rho_{\rm u}(a^2+v_{\rm u}^2)=\rho_{\rm m}(a^2+v_{\rm rms}^2). \quad (13)$$

The simplest ansatz for $\rho_{\rm m}$ and $v_{\rm rms}$ is that they depend only on the upstream Mach number,

$$\rho_{\rm m}/\rho_{\rm u} = \eta_1 M_{\rm u}^{\beta_1}, \quad (14)$$
$$v_{\rm rms}/a = \eta_2 M_{\rm u}^{\beta_2}. \quad (15)$$

Using the ansatz for $\rho_{\rm m}$ we obtain from Eq. 11 and 12 a first expression for $\kappa_{\rm 2d}$,

$$\kappa_{\rm 2d}=2a\eta_1^{-1}M_{\rm u}^{1-\beta_1}\propto aM_{\rm u}^{1-\beta_1}. \quad (16)$$

A second expression for $\kappa_{\rm 2d}$ we obtain from Eq. 13

$$\rho_{\rm u}a^2(1+M_{\rm u}^2)=\rho_{\rm m}(a^2+v_{\rm rms}^2)=\frac{a^2N}{\ell_{\rm cdl}}(1+\eta_2^2M_{\rm u}^{2\beta_2}). \quad (17)$$

Using again Eq. 12 to replace N one obtains

$$\kappa_{\rm 2d}=2aM_{\rm u}\frac{1+\eta_2^2M_{\rm u}^{2\beta_2}}{1+M_{\rm u}^2}\approx 2a\eta_2^2M_{\rm u}^{2\beta_2-1}\propto aM_{\rm u}^{2\beta_2-1}. \quad (18)$$

The approximation is good for high Mach number flows, with $\eta_2^2M_{\rm u}^{2\beta_2}>>1$, and for $\beta_2>0$ which is, however, to be expected for supersonic turbulence. Comparing Eq. 16 and 18 gives

$$\beta_2 = 1-\beta_1/2, \quad (19)$$
$$\eta_1^{-1} = \eta_2^2. \quad (20)$$

3.2.2. Driving energy

From energy conservation we have $\dot{\mathcal{E}}_{\rm diss}=\dot{\mathcal{E}}_{\rm drv}-\dot{\mathcal{E}}_{\rm kin}$. Here $\dot{\mathcal{E}}_{\rm drv}$ is the energy flux density entering the CDL per time and per unit length in y-direction. $\dot{\mathcal{E}}_{\rm diss}$ denotes the energy density dissipated per time within an average column of length $\ell_{\rm cdl}$ of the CDL. Finally, $\dot{\mathcal{E}}_{\rm kin}$ is the change per time of the kinetic energy contained within such an average column. We first turn to the driving energy $\dot{\mathcal{E}}_{\rm drv}$ and come back to $\dot{\mathcal{E}}_{\rm diss}$ and $\dot{\mathcal{E}}_{\rm kin}$ in Sect. 3.2.3.

Part of the total (left plus right) upwind kinetic energy flux density, $\mathcal{F}_{\rm e_{kin},u}=\rho_{\rm u}v_{\rm u}^3$, is thermalized at the shocks confining the CDL. The remaining part, $\dot{\mathcal{E}}_{\rm drv}$, drives the turbulence in the CDL. We assume that $\dot{\mathcal{E}}_{\rm drv}$ and $\mathcal{F}_{\rm e_{kin},u}$ are related by a function of the upwind Mach number only,

$$\dot{\mathcal{E}}_{\rm drv}=f_{\rm eff}(M_{\rm u})\mathcal{F}_{\rm e_{kin},u}. \quad (21)$$

We call the function $f_{\rm eff}$ the driving efficiency. An expression for $f_{\rm eff}$ can be derived by using the jump conditions for strong, oblique shocks,

$$\rho_{\rm d} = \rho_{\rm u}M_{\perp,\rm u}^2=\rho_{\rm u}M_{\rm u}^2\sin^2\alpha,$$
$$v_{\perp,\rm d} = v_{\perp,\rm u}M_{\perp,\rm u}^{-2}=\frac{a}{M_{\rm u}\sin\alpha},$$
$$v_{\parallel,\rm d} = v_{\parallel,\rm u}=aM_{\rm u}\cos\alpha. \quad (22)$$

The subscript d denotes downstream quantities, right after shock passage, the subscripts $\perp$ and $\parallel$ denote flow components perpendicular and parallel to the shock respectively, and α is given in Fig. 1. Using Eq. 22 we obtain

$$\dot{\mathcal{E}}_{\rm drv} = \frac{1}{\rm Y}\int_{s_{\rm l,r}} ds\frac{\rho_{\rm d}v_{\rm d}^2}{2}v_{\perp,\rm d} = \frac{\rho_{\rm u}v_{\rm u}^3}{2Y}\int_{\rm Y_{l,r}} dy(1-\sin^2\alpha+\frac{1}{M_{\rm u}^4\sin^2\alpha}), \quad (23)$$

where the integral over $s_{\rm l,r}$ and $\rm Y_{l,r}$ runs over both shocks, and where it was used that $\sin\alpha\ ds=dy$. The last term on the right hand side of Eq. 23 we omit in the following. This is justified as the shocks we observe in our simulations fulfill for the most part $\sin\alpha>>M_{\rm u}^{-2}$ (see Sect. 4.2.2). For $f_{\rm eff}(M_{\rm u})$ we thus obtain

$$f_{\rm eff}=\frac{1}{2Y}\int_{\rm Y_{l,r}}dy(1-\sin^2\alpha)\equiv 1-\sin^2\alpha_{\rm eff} \quad (24)$$

where we used the midpoint rule. The angle $\alpha_{\rm eff}$ can be interpreted as an average bending angle. As ansatz for the Mach number dependence of $f_{\rm eff}$ we thus take

$$f_{\rm eff}=1-\sin^2\alpha_{\rm eff}=1-\eta_3M_{\rm u}^{\beta_3}. \quad (25)$$

3.2.3. Energy dissipation

A first expression for the column integrated dissipated energy per time can be obtained from energy conservation, $\dot{\mathcal{E}}_{\rm diss}=\dot{\mathcal{E}}_{\rm drv}-\dot{\mathcal{E}}_{\rm kin}$. For $\dot{\mathcal{E}}_{\rm drv}$ we just derived an expression, Eqs. 21 and 25. For $\dot{\mathcal{E}}_{\rm kin}$ we obtain, within the frame of self-similarity,

$$\dot{\mathcal{E}}_{\rm kin}=\frac{\rho_{\rm m}v_{\rm rms}^2}{2}\frac{d\ell_{\rm cdl}}{dt}=\rho_{\rm u}a^3\frac{\eta_2}{2}M_{\rm u}^{3-\beta_1}, \quad (26)$$

where we used Eqs. 14, 15, and 18 to 20. Together we get

$$\dot{\mathcal{E}}_{\rm diss}=\rho_{\rm u}a^3M_{\rm u}^3\ [1-\eta_3M_{\rm u}^{\beta_3}-0.5\ \eta_2^2M_{\rm u}^{-\beta_1}]. \quad (27)$$

The energy dissipated per time within an average column of length $\ell_{\rm cdl}$ thus is independent of this length. If energy dissipation occurs only (as within the frame of Euler equations) or at least dominantly in shocks, this implies that the average distance between shocks increases and / or the average strength of the shocks decreases as the CDL grows.

A second expression for $\dot{\mathcal{E}}_{\rm diss}$ can be obtained from dimensional considerations. The energy dissipated per unit volume per unit time must be proportional to $\rho_{\rm diss}v_{\rm diss}^3\ell_{\rm diss}^{-1}$. Here, $\rho_{\rm diss}$, $v_{\rm diss}$, and $\ell_{\rm diss}$ are the characteristic density, velocity, and length scale of the dissipation. The energy dissipation within an average column of length $\ell_{\rm cdl}$ thus can be written as $\dot{\mathcal{E}}_{\rm diss}\propto\rho_{\rm diss}v_{\rm diss}^3\ell_{\rm diss}^{-1}\ell_{\rm cdl}$. As all length scales must evolve equally with time within the frame of self-similarity, $\ell_{\rm cdl}/\ell_{\rm diss}$ must be constant, thus

$$\dot{\mathcal{E}}_{\rm diss}\propto\rho_{\rm diss}v_{\rm diss}^3. \quad (28)$$

Comparison of Eq. 27 and Eq. 28 suggests $v_{\rm diss}\propto aM_{\rm u}$ and a more complicated Mach number dependence for

$\rho_{\rm diss}$. As $v_{\rm rms}$ is the only velocity scale we have, it seems natural to assume that $v_{\rm diss} \propto v_{\rm rms}$. It then follows that $v_{\rm rms} \propto a M_{\rm u}$ or $\beta_2 = 1$ (and $\beta_1 = 0$). We note that for a 1D case Gammie & Ostriker (1996) even found $v_{\rm diss} = v_{\rm rms}$.

3.3. Summary of expected scaling relations

If a self-similar solution exists we expect the following dependencies:

$$\rho_{\rm m} = \eta_1 \rho_{\rm u} M_{\rm u}^{\beta_1} = \eta_1 \rho_{\rm u}, \quad (29)$$

$$M_{\rm rms} = \eta_2 M_{\rm u}^{\beta_2} = \eta_1^{-1/2} M_{\rm u}, \quad (30)$$

$$\kappa_{\rm 2d} = \ell_{\rm cdl}/\tau = 2\eta_1^{-1} a M_{\rm u}, \quad (31)$$

$$\dot{\mathcal{E}}_{\rm drv} = \rho_{\rm u} a^3 M_{\rm u}^3 (1 - \eta_3 M_{\rm u}^{\beta_3}), \quad (32)$$

$$\dot{\mathcal{E}}_{\rm kin} = \rho_{\rm u} a^3 M_{\rm u}^3\, 0.5\, \eta_2^2, \quad (33)$$

$$\dot{\mathcal{E}}_{\rm diss} = \rho_{\rm u} a^3 M_{\rm u}^3 (1 - \eta_3 M_{\rm u}^{\beta_3} - 0.5\, \eta_2^2). \quad (34)$$

Note the differences to the 1D solution: Eq. 29 predicts the CDL mean density to be independent of $M_{\rm u}$ and $\kappa_{\rm 2d} \propto a M_{\rm u}$, in contrast to $\rho_{\rm 1d} \propto M_{\rm u}^2$ and $\kappa_{\rm 1d} \propto a/M_{\rm u}$.

In deriving the above relations, we have made four basic assumptions: a) we have simple Mach number dependencies of $\rho_{\rm m}$, $v_{\rm rms}$, and $f_{\rm eff}$, Eqs. 14, 15, and 25; b) the CDL density and velocity are uncorrelated; c) we have high Mach numbers in the sense that $\eta_2^2 M_{\rm u}^{2\beta_2} >> 1$ or $M_{\rm rms}^2 >> 1$; d) $v_{\rm diss} \propto v_{\rm rms}$.

In Sect. 4 we are going to check the validity of these assumptions and confront Eqs. 29 to 34 with numerically obtained values. We expect good agreement as long as $M_{\rm rms} >> 1$, thus dissipation in shocks likely dominates and as long as $\ell_{\rm cdl} << Y$. The 'Euler character' of the solution should prevail under these conditions. We are also going to determine those quantities that cannot be derived analytically. These are, on the one hand, the coefficients η_1 and η_3, as well as the exponent β_3. On the other hand, there are quantities for which we have no analytical expression at all, like the wiggling of the confining shocks, the associated distribution of the angle α, or the Mach number dependence of the length of the confining shocks.

4. Numerical results

4.1. Brief phenomenological description

We begin with a brief qualitative description of the CDL. As an example, the density structure of run R22_1.2.2 is shown in Fig. 3 for three different times.

A first characteristic is the local bending of the confining shocks. The spatial scale of these wiggles increases linearly with time, as the CDL accumulates more and more matter and gets more and more extended. The inclination of the wiggles with respect to the upstream flows increases with increasing upstream Mach number (see Sect. 4.2.2). Occasionally, we observe a superimposed 'bending mode' (e.g. bottom panel in Fig. 3), which in appearance is somewhat similar to the bending modes of the NTSI described by Vishniac (1994).

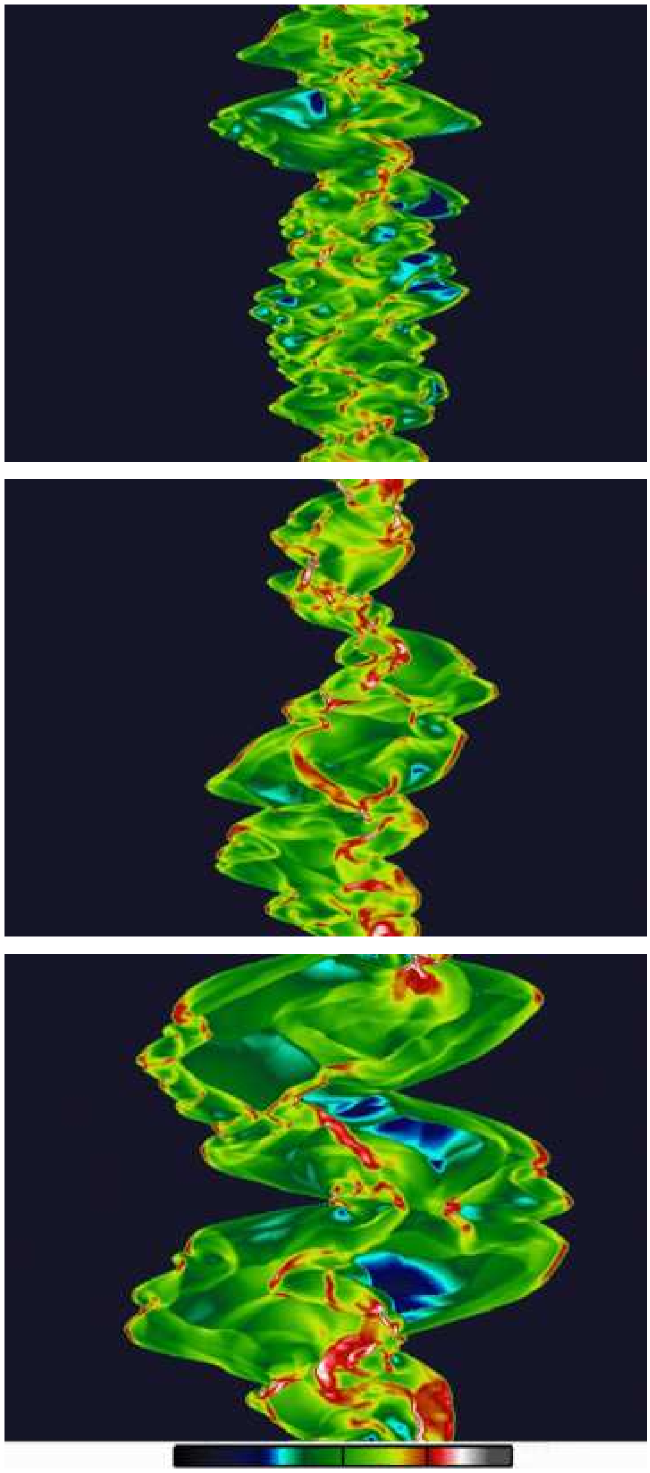

Fig. 3. The interaction zone of run R22_1.2.2, shown in density (logarithmic scale, in units of $\rho_{\rm u}$, color bar from 0 to 4), for three different times: $\ell(N) \approx 34$ (top), $\ell(N) \approx 54$ (middle), $\ell(N) \approx 74$ (bottom). The spatial scale of patches, filaments, and wiggling of the confining shocks increases with $\ell(N)$.

A second characteristic is the patchy appearance of the CDL. The turbulent interior is organized in filaments and patches, regions within which a flow variable remains more or less constant. The spatial extension of these patches increases as well as the CDL accumulates more and more matter. The flow variables clearly mirror the supersonic character of the turbulence: the contrast between high density filaments and extended patches in Fig. 3 easily reaches two orders of magnitude, the root mean square velocity is well above sound, and the mean density is substantially reduced compared to the 1D case. Shocks within the CDL are ubiquitous.

4.2. *Settings without CDL at* $t = 0$

For symmetric settings, and if there is no CDL at time $t = 0$, we expect to see the self-similar relations we derived in Sect. 3.2. The time evolution of the solution we express in terms of

$$\ell(N) \equiv N/N_0 = \frac{\rho_{\rm m}\ell_{\rm cdl}}{\rho_{\rm u}{\rm Y}_0}. \tag{35}$$

This function is monotonically increasing at about the same rate as the mean extension of the CDL, since $\rho_{\rm m} \approx \eta_1\rho_{\rm u}$ (Eq. 29). In fact, $\rho_{\rm m} \approx 30\rho_{\rm u}$ (Sect. 4.2.1) and thus $\ell(N) = 60$ corresponds to $\ell_{\rm cdl} \approx 2{\rm Y}_0$. For the symmetric case we consider in this paper $\ell(N)$ is proportional to the elapsed time. Using Eq. 12 to express N we can write

$$\ell(N) \equiv N/N_0 = \frac{2\tau\rho_{\rm u}v_{\rm u}}{\rho_{\rm u}{\rm Y}_0} = \tau\frac{2v_{\rm u}}{{\rm Y}_0}. \tag{36}$$

$\ell(N) = 60$ then corresponds to a time $\tau = 30Y_0/v_{\rm u}$. Or, if we use $v_{\rm u} \approx 5v_{\rm rms}$ (Sect. 4.2.1) and ${\rm Y}_0 \approx \ell_{\rm cdl}/2$ for $\ell(N) = 60$, we obtain $\tau \approx 3\ell_{\rm cdl}/v_{\rm rms}$.

Unless otherwise stated, averages and best fits in this section are always taken over the interval $10 \leq \ell(N) \leq 70$ and over all runs without CDL at time $t = 0$. The interval was chosen such that initialization effects have died away and that domain effects do not yet matter (Sect. 4.5.1).

We mention already here that the two most extreme simulations in terms of $M_{\rm u}$, R5_0.2.4 and R87_0.2.4, often differ somewhat from the other simulations. In the case of R5_0.2.4 we ascribe the deviation to the only subsonic turbulence and the correlation of density and velocity ($M_{\rm rms} \approx 0.9$ and ${\rm corr}(\rho, v) \approx -0.4$, see Sect. 4.2.1). In the case of R87_0.2.4, the shocks become sometimes too strongly inclined to be properly resolved by our numerical grid (Sect. 4.2.2).

4.2.1. CDL mean quantities and correlations

We first turn to the correlation of ρ and v and the CDL mean quantities $\rho_{\rm m}$ and $M_{\rm rms}$, Eqs. 29 and 30. One of our basic assumptions in deriving these self-similar relations, namely point b) that the CDL density and velocity are uncorrelated, we find confirmed by our simulations. For nearly all symmetric simulations without initial CDL and for $10 \leq \ell(N) \leq 70$ we have $0.1 \geq {\rm corr}(\rho, v) \geq -0.1$. The only exceptions are the three low Mach number runs R11_0.2.4, R11_0.2.2, and R5_0.2.4 with correlations of about -0.2, -0.2, and -0.4 respectively. Fig. 4, top panel, shows the time evolution of ${\rm corr}(\rho, v)$ for five selected runs which differ only in their upwind Mach number, $5 \leq M_{\rm u} \leq 90$.

In the same figure, middle and bottom panel, $\rho_{\rm m}/\rho_{\rm u}$ and $M_{\rm rms}/M_{\rm u}$ are shown as a function of $\ell(N)$ for the same runs. Two things are apparent. First, the ratios take similar values for all five runs, indicating for the exponents in Eqs. 29 and 30 that indeed $\beta_1 \approx 0$ and $\beta_2 \approx 1$. Second, the ratios are not constant with $\ell(N)$, indicating that the numerical solution is indeed only approximately self-similar. We come back to this point in Sect. 5.

To determine optimum exponents $\beta_{\rm i}$, $i = 1, 2$, we rewrite Eqs. 29 and 30 as equations for η_1 and η_2 and minimize the variance $\sigma^2(\eta_{\rm i})$. Considering all data points within $10 \leq \ell(N) \leq 70$ of all runs without a CDL at $t = 0$, we find the smallest variances for $\beta_1 = 0$ and for $\beta_2 = 1$. The corresponding means are $\mu(\eta_1) \approx 28$ and $\mu(\eta_2) \approx 0.21$. Although clearly identifiable, the minima of σ are relatively shallow. Changing β_1 or β_2 by ± 0.1, or excluding the very low Mach number case R5_0.2.4 (for which $M_{\rm rms} \approx 0.9$) changes σ by only about 5%. Repeating the analysis but allowing for a linear dependence of $\eta_{\rm i}$ on $\ell(N)$, we obtain the same optimum values for β_1 and β_2 but with considerably smaller variance. As $\ell(N)$ increases from 10 to 70, η_1 augments by about 25% (from 25 to 31), while η_2 decreases by about 15% (from 0.22 to 0.19).

Part of our assumption a), namely the simple Mach number dependencies of $\rho_{\rm m}$ and $M_{\rm rms}$, thus seems justified. With $\eta_2 = 0.21$ assumption c), $\eta_2^2 M_{\rm u}^2 >> 1$, is also fulfilled for most of our simulations. An exception is again run R5_0.2.4, for which $\eta_2^2 M_{\rm u}^2 \approx 1$.

In summary, the simulation results, $\rho_{\rm m} \approx 28\rho_{\rm u}$ and $M_{\rm rms} \approx 0.21 M_{\rm u}$, essentially confirm the expected relations, Eqs. 29 and 30. $\eta_1^{1/2}\eta_2 = 1$, predicted by Eq. 20, is fulfilled to within 10% at any given time. The mean density is (nearly) independent of $M_{\rm u}$. As expected, the solution is only approximately self-similar, $M_{\rm rms}$ decreases by about 15% as $\ell(N)$ increases from 10 to 70.

4.2.2. Confining shocks

The turbulence within the CDL is driven by the upstream flows. The confining shocks of the CDL affect this driving in two ways. The more inclined the shocks are on average with respect to the upstream flows, (smaller angle $\alpha_{\rm eff}$ in Eq. 24), the more kinetic energy survives shock passage and is available for driving the turbulence. The smaller the spatial scale on which the angle α varies, the smaller the scale on which the energy input changes. In the following, we analyze how these shock properties depend on $M_{\rm u}$ and on $\ell_{\rm cdl}$.

For this purpose, we specify the following basic quantities. The discrete x-position of the left and right shock, $s_{\rm l}$ and $s_{\rm r}$, we define for each discrete y-position y_j as the two cell boundaries where the Mach number drops for the

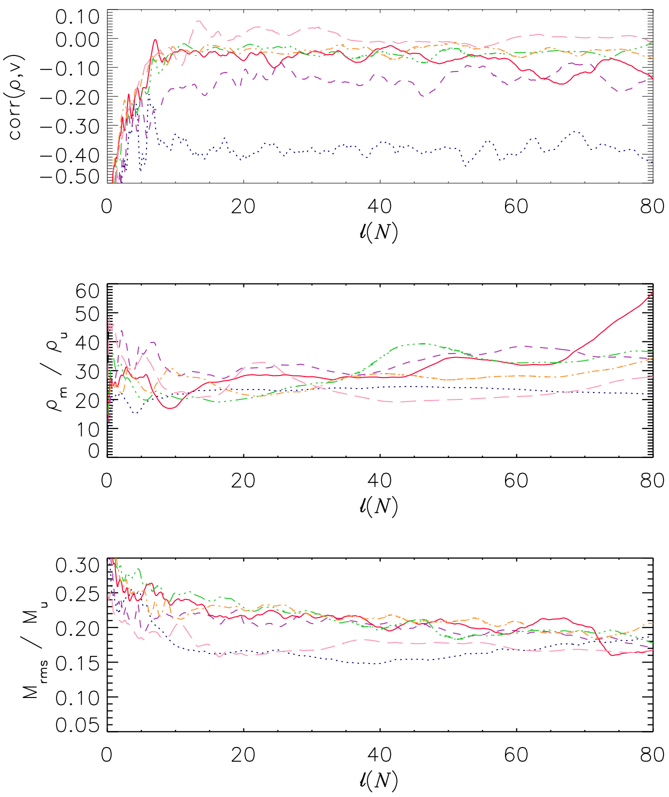

Fig. 4. Time evolution of $\mathrm{corr}(\rho, v)$ (top), $\rho_{\mathrm{m}}/\rho_{\mathrm{u}}$ (middle), and $M_{\mathrm{rms}}/M_{\mathrm{u}}$ (bottom) for runs R5_0.2.4 (dotted, dark blue), R11_0.2.4 (dashed, purple), R22_0.2.4 (solid, red), R33_0.2.4 (dash-dotted, orange), R43_0.2.4 (dash-three-dots, green), and R87_0.2.4 (long dashes, pink). For these runs, $\ell(N) = 60$ corresponds to $\ell_{\mathrm{cdl}} \approx \mathrm{Y}/2$.

first time from its upwind value M_u to $0.8M_u$. The average extension of the CDL, ℓ_{cdl}, we determine as

$$\ell_{\mathrm{cdl}} = \frac{1}{J}\sum_{j=1}^{J}[s_{\mathrm{r}}(y_j) - s_{\mathrm{l}}(y_j)]. \tag{37}$$

The length of the left and right shock, $\ell_{\mathrm{sh,l}}$ and $\ell_{\mathrm{sh,r}}$, we compute as

$$\ell_{\mathrm{sh,i}} = \sum_{j=1}^{J}[(s_{\mathrm{i}}(y_j) - s_{\mathrm{i}}(y_{j-1}))^2 + (y_j - y_{j-1})^2]^{1/2}. \tag{38}$$

J is the number of cells in y-direction, and $i = l, r$. The angle $\alpha_{\mathrm{l,r}}(y_j)$ we define as the angle between the x-axis and the tangent to the shock (see Fig. 1). Its numerical computation is described in Appendix A. To obtain a number distribution we sort the values $\alpha_{\mathrm{l,r}}(y_j) \in [0, \pi/2]$ into 60 bins. Finally, to obtain a measure for the scale on which the shocks are wiggled we look at the auto-correlation functions $\Gamma_{\mathrm{l,r}}$,

$$\Gamma_{\mathrm{i}}(y_{\mathrm{corr}}) = \frac{< [s_{\mathrm{i}}(y_j) - \bar{s}_{\mathrm{i}}] \cdot [s_{\mathrm{i}}(y_j + y_{\mathrm{corr}}) - \bar{s}_{\mathrm{i}}] >}{\sigma_{\mathrm{s}}^2}. \tag{39}$$

σ_{s}^2 is the variance of the shock position s_{i}, $< . >$ denotes the mean over all discrete position y_j. For each time, we determine $y_{\mathrm{corr_0}}$ such that $\Gamma_{\mathrm{i}}(y_{\mathrm{corr_0}}) = 0.5$. Averaging $y_{\mathrm{corr_0}}$ over both shocks gives a mean auto-correlation length ℓ_{corr},

$$\ell_{\mathrm{corr}} = \frac{1}{2}\left[y_{\mathrm{corr_0}}(s_{\mathrm{l}}) + y_{\mathrm{corr_0}}(s_{\mathrm{r}})\right]. \tag{40}$$

A larger auto-correlation length ℓ_{corr} then indicates that the shocks are wiggled on a larger spatial scale, but it does not give the scale of the wiggles in absolute units (see below).

All four quantities, CDL extension, number distribution of angle α, shock length, and correlation length, are shown in Fig. 5.

Fig. 5, first panel, shows the essentially linear growth of the CDL with $\ell(N)$. The growth rate is, however, slowly decreasing with increasing $\ell(N)$. The slope of a linear fit in the range $40 < \ell(N) < 70$ is roughly 10% smaller than the slope obtained in the range $10 < \ell(N) < 40$. This fits with the slight increase in ρ_{m}, observable in Fig. 4, middle panel.

Fig. 5, second panel, shows that the average shock length $\ell_{\mathrm{sh}} = 0.5(\ell_{\mathrm{sh,l}} + \ell_{\mathrm{sh,r}})$, is fairly constant with respect to $\ell(N)$ but increases with M_{u}. Assuming a dependence of the form $\ell_{\mathrm{sh}} = \eta_{\mathrm{sh}} \mathrm{Y} M_{\mathrm{u}}^{\beta_{\mathrm{sh}}}$, the variance $\sigma^2(\eta_{\mathrm{sh}})$ becomes minimal for $\beta_{\mathrm{sh}} = 0.8$. As can be seen, the two runs R5_0.2.4 and R87_0.2.4 again behave somewhat differently. Neglecting these two runs β_{sh} remains unchanged but σ is reduced by about 40%.

Fig. 5, third panel, shows that larger upwind Mach numbers lead to more inclined shocks with respect to the upstream flows (smaller values of α). Shown is the number distribution of α, averaged over $10 \leq \ell(N) \leq 70$. Individual runs show a slight shift towards larger values of α as $\ell(N)$ increases. This shift is, however, small compared to the effect of M_{u}.

Fig. 5, fourth panel, shows the auto-correlation length ℓ_{corr}. It depends not only on M_{u} but is also proportional to ℓ_{cdl}. The best fit is found to be $\ell_{\mathrm{corr}} \approx 0.7 \ell_{\mathrm{cdl}} M_{\mathrm{u}}^{-0.6}$. Fig. 5, fifth panel, shows ℓ_{corr} scaled with this best fit. From these scaling properties of ℓ_{corr} we take that larger values of M_{u} lead to smaller scale wiggling of the shocks relative to ℓ_{cdl}.

The absolute value of ℓ_{corr} clearly depends on the choice of the threshold value in our definition, $\Gamma(y_{\mathrm{corr}}) = 0.5$. Fig. 6 illustrates the variation of Γ_{l} as a function of y_{corr} at the example of run R43_0.2.4. Fig. 6, top panel, shows that the initially present sinusoidal wiggling of the confining shocks does not get lost until about $\ell(N) = 15$, which is rather late compared to the other runs. Mode-like signatures appear again around $\ell(N) \gtrsim 50$. Our data give, however, no clear answer on how typical and persistent such signatures are. A basic problem is that their wave-length soon becomes comparable (within a factor of 2 or so) to the domain size in y-direction, which may affect the signatures. From Fig. 6, bottom panel, it can be taken, on the other hand, that Γ_{l} decreases essentially linearly from 1 to about 0.2. The other simulations show a similar behavior. Consequently, the above scaling proper-

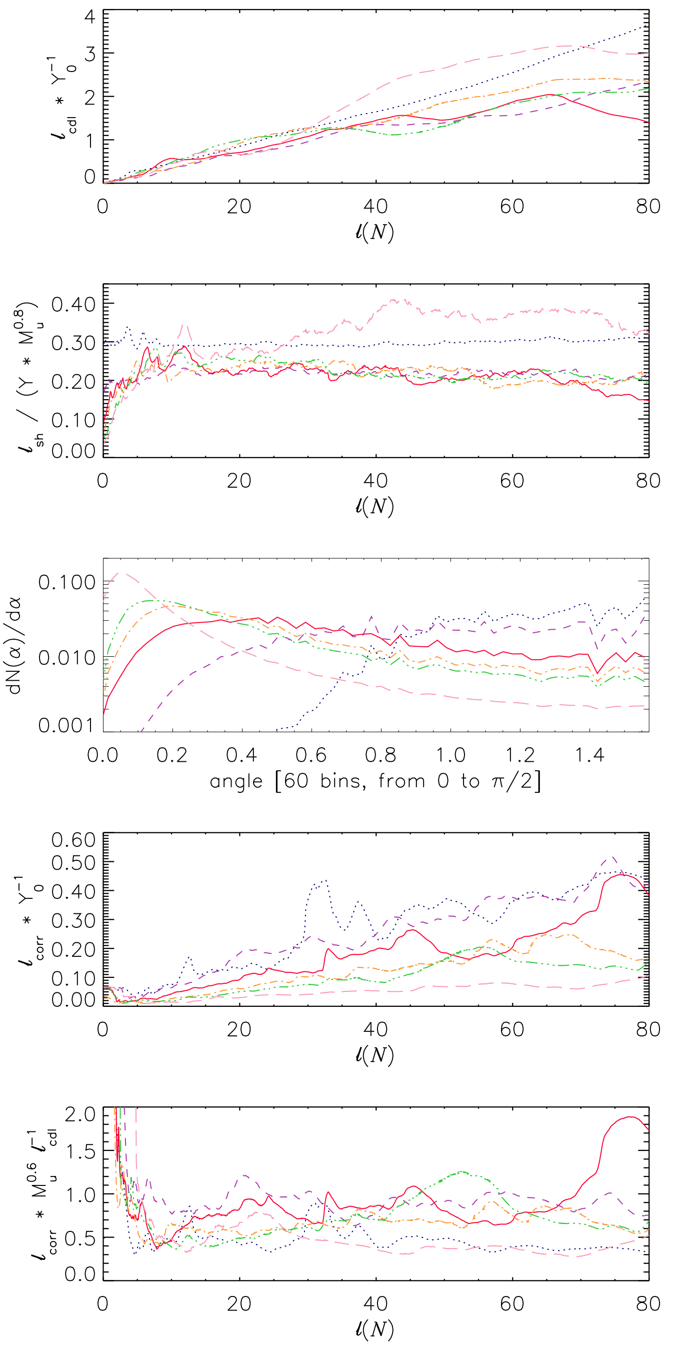

Fig. 5. Quantities related to the confining shocks. Average extension ℓ_{cdl} of the CDL (first panel), total normalized shock length, $l_{\mathrm{sh}}/(\mathrm{Y}M_{\mathrm{u}}^{0.8})$, (second panel), Number distribution (60 bins) of obliqueness angle α, averaged over $10 \leq \ell(N) \leq 70$ (third panel), auto-correlation length, $\ell_{\mathrm{corr}}/\mathrm{Y}_0$ (fourth panel), and scaled auto-correlation length, $\ell_{\mathrm{corr}}/(\ell_{\mathrm{cdl}} M_{\mathrm{u}}^{-0.6})$, (fifth panel). Individual curves denote the same runs as in Fig. 4.

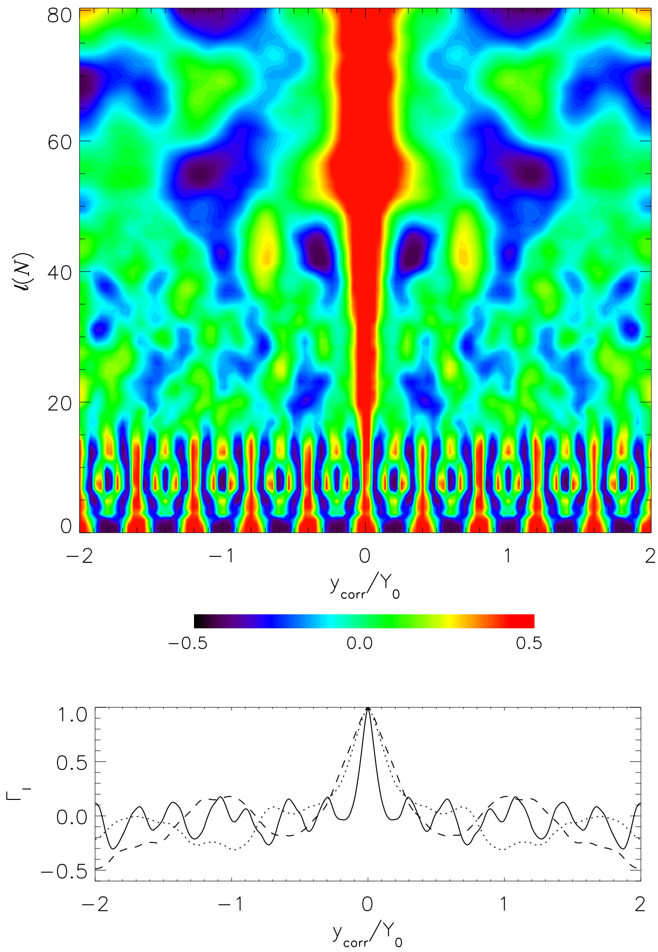

Fig. 6. Variation of Γ_1, color coded, as a function of y_{corr} for run R43_0.2.4 (top panel). To allow for better display the color scale is limited to a range $-0.5 \leq \Gamma_1 \leq +0.5$. Smaller or larger values of Γ_1 are uniformly colored in dark blue or red, respectively. For the same run, Γ_1 is shown as a function of y_{corr} for three selected times (bottom panel). $\ell(N) = 30$ (solid), $\ell(N) = 50$ (dotted), $\ell(N) = 70$ (dashed).

ties of ℓ_{corr} should also be obtained if smaller threshold values are used, down to about $\Gamma(y_{\mathrm{corr}}) = 0.2$.

Fig. 4 and Fig. 5 also allow some insight as to why runs R5_0.2.4 and R87_0.2.4 sometimes fit not so well. Fig. 5, third panel, shows that for run R87_0.2.4, the largest upwind Mach number we have considered, our spatial resolution is barely sufficient. The number distribution here peaks at around $\alpha \approx 0.1$. In terms of discrete positions this means that the shock position changes by about 15 cells in x-direction as one moves from y_j to y_{j+1}. Run R5_0.2.4, on the other hand, may just deviate because of its low Mach number. The turbulence within its CDL is subsonic, $M_{\mathrm{rms}} \approx 0.9$, and with $\eta_2^2 M_{\mathrm{u}}^2 \approx 1.1$ and $\mathrm{corr}(\rho, v) \approx -0.4$ (Fig. 4, top panel) it violates two of the basic assumptions made when deriving the self-similar scaling laws in Sect. 3.2.

In summary, as M_{u} increases, the bounding shocks become more inclined with respect to the upstream flows (smaller α), the fraction of upstream kinetic energy that survives the passage through the bounding shocks increases, and the bounding shocks themselves are wiggled on progressively smaller scales (smaller $\ell_{\mathrm{corr}}/\ell_{\mathrm{cdl}}$.

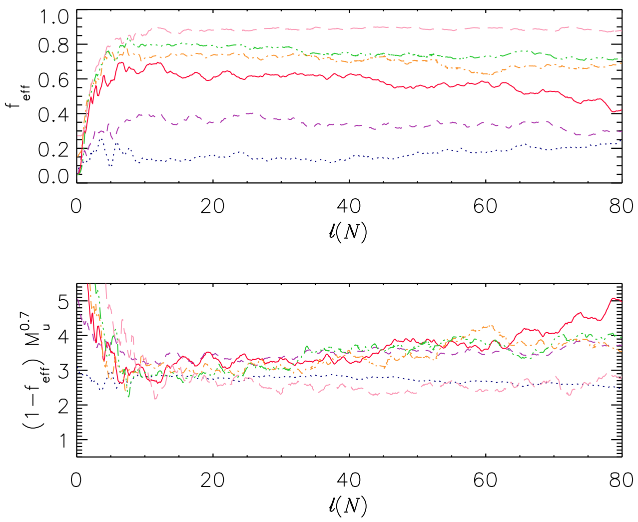

Fig. 7. Driving efficiency (top panel) and best fit $\eta_3 = (1 - f_{\rm eff}) M_{\rm u}^{0.7}$ (bottom panel). For details see text.

4.2.3. Energy balance

Energy input into the CDL occurs only at its confining interfaces. Energy dissipation, on the other hand, occurs throughout the CDL volume. Nevertheless, according to the analysis in Sect. 3.2 both $\dot{\mathcal{E}}_{\rm drv}$ and $\dot{\mathcal{E}}_{\rm diss}$ should be independent of the CDL extension if dissipation is due to shocks only and if $\ell_{\rm cdl}$ is small compared to Y. The average distance between shocks then must increase and / or the average strength of the shocks must decrease as the CDL grows.

To determine $\dot{\mathcal{E}}_{\rm drv}$ we must compute the driving efficiency $f_{\rm eff} = \dot{\mathcal{E}}_{\rm drv}/\mathcal{F}_{\rm e_{kin},u}$. The corresponding integral in Eq. 24 we evaluate numerically, the resulting driving efficiency is shown in Fig. 7, top panel. As can be seen, larger Mach numbers lead to more efficient driving, a smaller part of the upstream kinetic energy is thermalized already at the confining shocks. The driving efficiency $f_{\rm eff}$ increases by about a factor of four between runs R5_0.2.4 and R87_0.2.4. Also noteworthy, the absolute value of the driving power $\dot{\mathcal{E}}_{\rm drv}$ differs by more than 4 orders of magnitude between runs R5_0.2.4 and R87_0.2.4. The best fit for the assumed Mach number dependence (minimization of $\sigma(\eta_3)$ in Eq. 25) yields $\beta_3 = -0.7$. The corresponding values of $\eta_3 = (1 - f_{\rm eff}) M_{\rm u}^{0.7}$ are shown in Fig. 7, bottom panel. From the figure we take that the second part of our assumption a), the simple Mach number dependence of $f_{\rm eff}$, seems justified. The figure also shows that $f_{\rm eff}$, and thus the driving power $\dot{\mathcal{E}}_{\rm drv}$, is not strictly independent of $\ell_{\rm cdl}$ but decreases with increasing $\ell(N)$. Repeating the best fit analysis but allowing for a linear dependence of η_3 on $\ell(N)$ leads again to $\beta_3 = -0.7$, while η_3 changes from 3.1 to 3.6 as $\ell(N)$ goes from 10 to 70. The average value of η_3 is 3.3. Omission of the extreme runs R5_0.2.4 and R87_0.2.4 does not change the result.

The dissipated energy we determine as $\dot{\mathcal{E}}_{\rm diss} = \dot{\mathcal{E}}_{\rm drv} - \dot{\mathcal{E}}_{\rm kin}$ (Sect. 3.2.2), where $\dot{\mathcal{E}}_{\rm kin}$ is the change per time of the kinetic energy within an average column of the CDL. $\dot{\mathcal{E}}_{\rm kin}$ we get directly from our simulation data. Fig. 8 shows the numerically obtained value $\dot{\mathcal{E}}_{\rm diss}$ (top panel) and the theoretically expected value (Eq. 34) $\dot{\mathcal{E}}_{\rm diss}^{\rm th}$ (middle panel), both in units of $\mathcal{F}_{\rm e_{kin},u} = \rho_{\rm u} v_{\rm u}^3$, as well as the ratio of the two (bottom panel). For better display, the theoretical value, which must not depend on $\ell(N)$, is shown as a (constant) function of $\ell(N)$. For the constants in Eq. 34 we used the

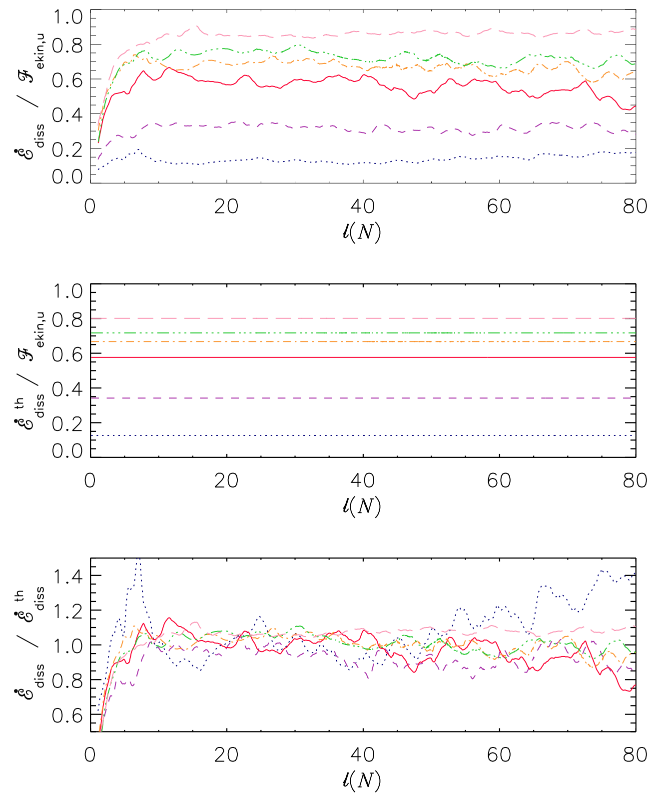

Fig. 8. Numerically obtained (top panel) and theoretically expected (middle panel) energy dissipation in units of the upstream kinetic energy flux density $\mathcal{F}_{\rm e_{kin},u} = \rho_{\rm u} v_{\rm u}^3$. The constants in Eq. 34 were set to the best fit values, $\eta_3 = 3.3$, $\beta_3 = -0.7$, and $\eta_2 = 0.21$. Only for run R5_0.2.4 we used $\eta_3 = 2.75$ (for details see text). The bottom panel shows the ratio of the two quantities. Individual curves denote the same runs as in Fig. 4. For better display $\dot{\mathcal{E}}_{\rm diss}$ was smoothed using a running mean with time window $\Delta\ell(N) = \pm 1$.

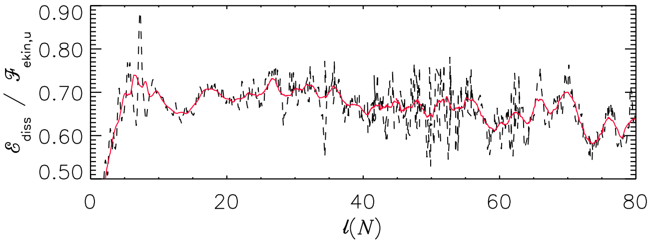

Fig. 9. Effect of smoothing $\dot{\mathcal{E}}_{\rm diss}$ with a running mean and window $\Delta\ell(N) = \pm 1$, illustrated at the example of run R33_0.2.4. Shown is $\dot{\mathcal{E}}_{\rm diss}$ in units of $\mathcal{F}_{\rm e_{kin},u} = \rho_{\rm u} v_{\rm u}^3$, before (dashed, black) and after (solid, red) smoothing, in units of erg cm^{-3}s^{-1}.

numerically obtained average values, $\eta_3 = 3.3$, $\beta_3 = -0.7$, and $\eta_2 = 0.21$. Only for R5_0.2.4 we used $\eta_3 = 2.75$, in accordance with Fig. 7, bottom panel. Also for better display, the numerically obtained value was smoothed using a running mean with window size $\Delta\ell(N) = \pm 1$. The effect of the smoothing is illustrated in Fig. 9 at the example of run R11_0.2.4.

Looking at the data of $\dot{\mathcal{E}}_{\rm diss}$ and $\dot{\mathcal{E}}_{\rm drv}$, three points may be stressed. First, $\dot{\mathcal{E}}_{\rm diss}$ (Fig. 8, top panel) mirrors $\dot{\mathcal{E}}_{\rm drv} = \mathcal{F}_{\rm e_{kin},u} f_{\rm eff}$ (Fig. 7, top panel), the values usually differ by less than 10%. This is not surprising. It implies, however, that for larger upstream Mach numbers a larger the fraction of the upstream kinetic energy is thermalized only within the volume of CDL, and not already at its confining shocks. For $M_{\rm u} \gtrsim 20$, the energy dissipated within the CDL exceeds 50% of the upstream kinetic energy (Fig. 8, top panel).

Second, Fig. 8, bottom panel, shows that $\dot{\mathcal{E}}_{\rm diss}^{\rm th}$ and $\dot{\mathcal{E}}_{\rm diss}$ agree to within 10% most of the time. Given the large range covered (5 orders of magnitude in $\dot{\mathcal{E}}_{\rm diss}$, a factor of 20 in $M_{\rm u}$, and an increase by a factor of 7 in $\ell(N)$), we conclude that the self-similar solution gives a good estimate.

Third, from the same figure it can be seen that $\dot{\mathcal{E}}_{\rm diss}$ generally decreases, except for run R5_0.2.4. Excluding R5_0.2.4, a linear fit to $\dot{\mathcal{E}}_{\rm diss}/\dot{\mathcal{E}}_{\rm diss}^{\rm th}$ yields a decreases of 10% as $\ell(N)$ increases from 10 to 70. A similar fit to $\dot{\mathcal{E}}_{\rm drv}/\dot{\mathcal{E}}_{\rm drv}^{\rm th}$, with $\dot{\mathcal{E}}_{\rm drv}^{\rm th} = \rho_{\rm u} v_{\rm u}^3 (1 - 3.3 M_{\rm u}^{-0.7})$ yields an even slightly larger decrease of 13%. The net dissipation, $\dot{\mathcal{E}}_{\rm diss}/\dot{\mathcal{E}}_{\rm drv}$, in fact increases by 3%. Thus, as the CDL size increases, the absolute dissipation within an average column decreases while the net dissipation increases.

In summary, the predicted scaling laws, Eqs. 32 to 34, are – within the range of applicability – essentially confirmed by the simulations. The fraction of upstream kinetic energy dissipated only within the CDL, and not at the confining shocks, thus increases with $M_{\rm u}$. Best fit analysis for the numerical constants yields $f_{\rm eff} = 1 - 3.3\ M_{\rm u}^{-0.7}$. Both $\dot{\mathcal{E}}_{\rm drv}$ and $\dot{\mathcal{E}}_{\rm diss}$ slightly decrease with increasing $\ell_{\rm cdl}$. The net dissipation rate $\dot{\mathcal{E}}_{\rm diss}/\dot{\mathcal{E}}_{\rm drv}$ increases, but only slightly (3% increase as $\ell(N)$ goes from 10 to 70.)

4.2.4. Length scales of the turbulence

In Sect. 4.2.2 we looked at the scaling properties of the confining shocks. We pointed out that smaller autocorrelation lengths $\ell_{\rm corr}$ imply smaller scale wiggling, thus smaller scale changes of the kinetic energy entering the CDL. In the following, we show that the interface based quantity $\ell_{\rm corr}$ is proportional to the length scale derived from the volume properties of the turbulence. We take this as evidence for the tight coupling between volume and interface properties, between the turbulence and its driving.

On dimensional grounds, we can define two length scales based on volume properties of the turbulence,

$$\ell_{\rm e_{kin}} \equiv \frac{N^{-1/2} \mathcal{E}_{\rm kin}^{3/2}}{\dot{\mathcal{E}}_{\rm diss}}, \tag{41}$$

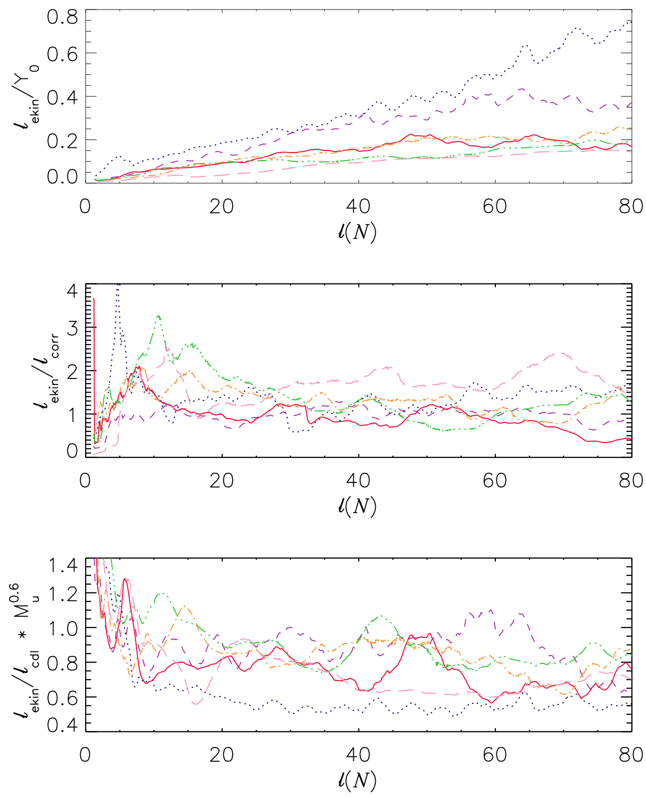

Fig. 10. Characteristic length $\ell_{\rm e_{kin}}$ of the turbulence (top), relative to $\ell_{\rm corr}$ (middle), and scaled with best fit $\ell_{\rm cdl} M_{\rm u}^{0.6}$ (bottom) as functions of $\ell(N)$. Individual curves denote the same runs as in Fig. 4. For better display $\ell_{\rm e_{kin}}$ was smoothed by a running mean with window $\Delta\ell(N) = \pm 1$.

$$\ell_{\rm v_{rms}} \equiv \frac{N v_{\rm rms}^3}{\dot{\mathcal{E}}_{\rm diss}}, \tag{42}$$

where $\mathcal{E}_{\rm kin} = \frac{\ell_{\rm cdl}}{2V} \int_{\rm V} \rho v^2$ is the average column integrated kinetic energy density. V here is again the 2D volume of the CDL, introduced in Sect. 2.3.1. The two scales are equal up to a numerical constant if the density and velocity are uncorrelated, in which case we can replace the average over the product ρv^2 by the product of the averages of ρ and v^2, $\mathcal{E}_{\rm kin} = \ell_{\rm cdl} \rho_{\rm m} v_{\rm rms}^2 = N v_{\rm rms}^2$. As this is the case in most of our simulations we look at only one of the above quantities in the following, $\ell_{\rm e_{kin}}$, shown in Fig. 10, top panel. For better display, as $\ell_{\rm e_{kin}}$ inherits the large time variability of $\dot{\mathcal{E}}_{\rm diss}$, it was smoothed in the same way as $\dot{\mathcal{E}}_{\rm diss}$ in Fig. 8, bottom panel.

Assuming a relation of the form $\ell_{\rm e_{kin}} = \alpha_{\rm e_{kin}} \ell_{\rm corr}$ we obtain optimal fits (minimum of $\sigma^2(\alpha_{\rm e_{kin}})$) for $\alpha_{\rm e_{kin}} \approx 1.3$. The fits become only slightly better if a weak linear dependence of $\alpha_{\rm e_{kin}}$ on $\ell(N)$ is allowed (13% change as $\ell(N)$ goes from 10 to 70). $\ell_{\rm e_{kin}}/\ell_{\rm corr}$ is shown in Fig. 10, middle panel.

Looking directly at the dependence of $\ell_{\rm e_{kin}}$ on $\ell_{\rm cdl}$ and $M_{\rm u}$ we find $\ell_{\rm e_{kin}} \propto \ell_{\rm cdl} M_{\rm u}^{-0.6}$. This is the same dependence we found for $\ell_{\rm corr}$ in Sect. 4.2.2. $\ell_{\rm e_{kin}}$ scaled with this best fit is shown in Fig. 10, bottom panel.

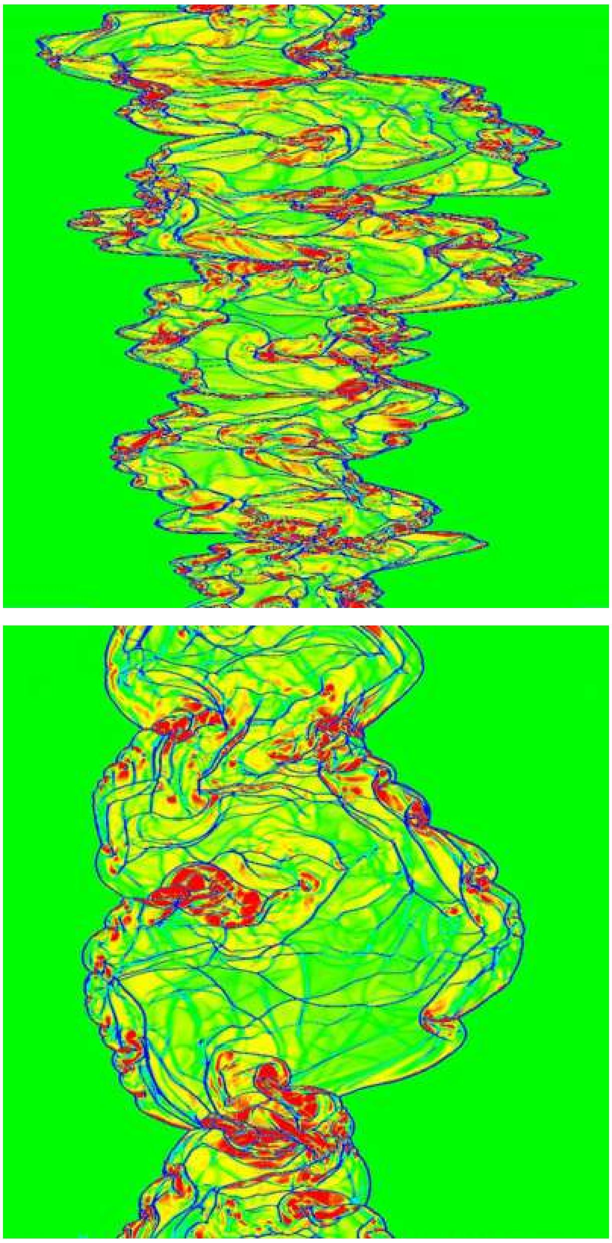

Fig. 11. Plots of div($\boldsymbol{v}$) for two runs that are identical except for their upstream Mach number. Larger upstream Mach numbers lead, on average, to finer structure within the CDL and smaller scale wiggling of the confining shocks. Shown are run R33_0.2.4 (top) and run R11_0.2.4 (bottom), both at a time where $\ell_{\rm cdl} \approx 2\,{\rm Y}_0 = {\rm Y}/2$. Blue (dark lines) indicates convergence, red (dark patches) divergence.

With increasing upstream Mach number the characteristic length scale $\ell_{e_{\rm kin}}$ thus decrease relative to the CDL extension. This is consistent with our observation that for the same $\ell_{\rm cdl}$ the interior of the CDL shows finer structuring (patches, filaments) for larger values of $M_{\rm u}$. Fig. 11 illustrates this observation at the example of runs R11_0.2.4 and R33_0.2.4. Shown in the figure is div($\boldsymbol{v}$), as the flow patterns, especially shocks, are better visible in this quantity than in density.

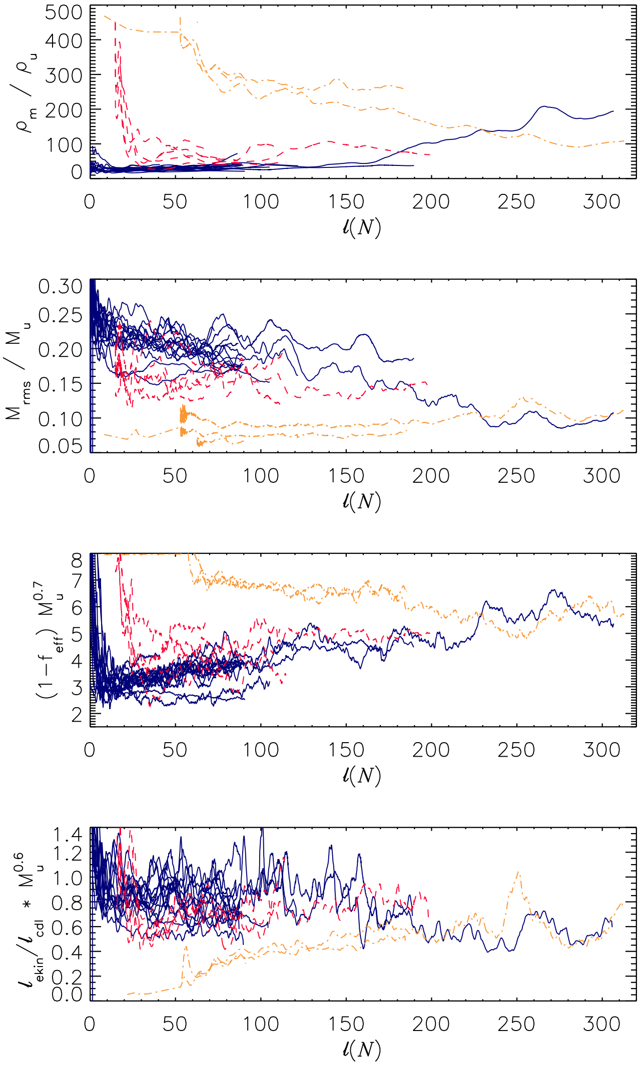

Fig. 12. Comparing runs with and without an initial CDL. Shown are $\rho_{\rm m}/\rho_{\rm u}$ (first), $M_{\rm rms}/M_{\rm u}$ (second), the scaled driving efficiency $(1-f_{\rm eff})M_{\rm u}^{0.7}$ (third), and the scaled characteristic length of the turbulence $\ell_{e_{\rm kin}}/\ell_{\rm cdl}\cdot M_{\rm u}^{0.6}$ for all symmetric runs. Line styles and colors denote initial conditions, 0 (solid line, blue), 1 (dashed line, red), and 2 (dash-dotted line, orange).

In summary, our simulations show that the inherent length scale of the turbulence is proportional to the autocorrelation length of the confining shocks, independent of $M_{\rm u}$ and $\ell_{\rm cdl}$. With increasing $M_{\rm u}$, both length scales decrease relative to the CDL extension, $\ell_{e_{\rm kin}}/\ell_{\rm cdl} \propto M_{\rm u}^{-0.6}$. The appearance of the CDL, the size of its patches and filaments, behaves similarly.

4.3. Settings with CDL at $t = 0$

We performed additional runs to study the influence of an initially present CDL. Fig. 12 illustrates the results at some selected quantities. Shown are all the runs we have performed with initial condition I=0 (solid blue, no CDL at $t = 0$), I=1 (dashed red, moderate CDL at $t = 0$), and I=2 (dash-dotted orange, massive CDL at $t = 0$).

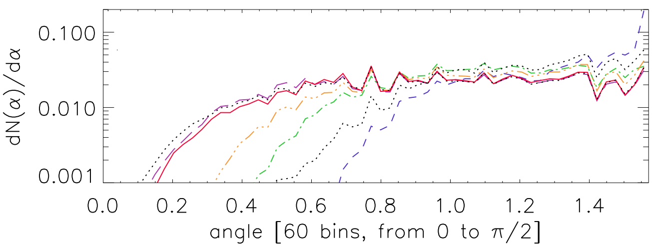

Fig. 13. Time evolution of angle distribution for run R22_2.2.2. Shown is the average angle distribution for $10 < \ell(N) < 70$ (dashed, blue), $70 < \ell(N) < 130$ (dash-dotted, green), $130 < \ell(N) < 190$ (dash-three-dots, orange), $190 < \ell(N) < 250$ (long dashes, purple), $250 < \ell(N) < 310$ (solid, red). Also shown are the distributions for run R5_0.2.4 (black dots, right line) and for run R11_0.2.4 (black dots, left line), both averaged over $10 < \ell(N) < 70$.

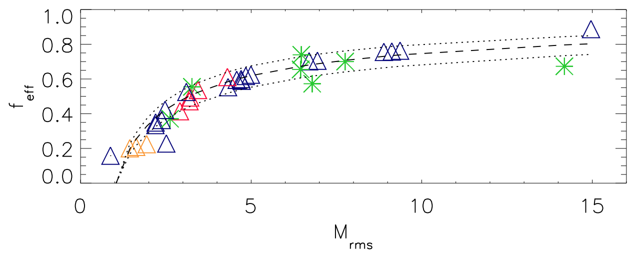

Fig. 14. Average $f_{\rm eff}$ as a function of $M_{\rm rms}$ for all our symmetric simulations (triangles). In addition, we included data from our asymmetric runs (asterisks), for which $1.6M_{\rm r} \leq M_{\rm l} \leq 64M_{\rm r}$ and which have no CDL initially. Averages were taken over $10 \leq \ell(N) \leq 70$ for simulations without initial CDL (blue triangles and green asterisks), over $40 \leq \ell(N) \leq 70$ for runs with a moderate initial CDL (red triangles), and over $70 \leq \ell(N) \leq 140$ for runs with a massive initial CDL (orange triangles). Lines show $f_{\rm eff} = 1 - M_{\rm rms}^{\xi}$ with $\xi = -0.6$ (dashed) and $\xi = -0.6 \pm 0.1$ (dotted).

Comparison of the red (I=1) and blue (I=0) curves in Fig. 12 shows that an initially present CDL of moderate column density ($N = 14\,N_0$) soon develops characteristics similar to those found in simulations without initial CDL. A quasi-steady state is reached for $\ell(N) \gtrsim 40$. The red and blue curves then agree to within about a factor of two for volume quantities like $\rho_{\rm m}$ and $M_{\rm rms}$ (first two panels in Fig. 12). Agreement seems slightly better for interface related quantities. For $(1 - f_{\rm eff})\,M^{0.7}$, shown in the third panel of Fig. 12, the red and blue curves lie more or less on top of each other. The same is true for $\ell_{\rm e_{kin}}/\ell_{\rm cdl}\,M_{\rm u}^{0.6}$, shown in the bottom panel of Fig. 12.

The situation is slightly different for runs with an initially rather massive CDL (I=2, with initially $N = 56\,N_0$). Also in these simulations, represented by the orange curves in Fig. 12, the CDL gets more and more turbulent. For all the quantities shown in Fig. 12, the orange curves approach the blue and red curves. However, it takes these runs much longer to saturate. Only for $\ell(N) > 240$ the curves finally seem to saturate, at similar values as the blue and red curves. That saturation indeed occurs around that time is also supported by Fig. 13. As can be seen, the average angle distribution of the confining shocks for run R22_2.2.2 first shifts to larger and larger values as $\ell(N)$ increases. It then stagnates for the last two averaging periods, $190 < \ell(N) < 250$ and $250 < \ell(N) < 310$.

In summary, we conclude that our symmetric simulations all end up in a similar quasi-steady final state. An initially present CDL only delays the development. The incoming flows manage to generate (and sustain) a similar level of turbulence also within an initially massive CDL.

4.4. Asymmetric cases

We also computed a few asymmetric cases already, where the two upwind Mach numbers are different, $M_{\rm l} \neq M_{\rm r}$. For the same reason as given in Sect. 3, we expect the solution to depend only on $M_{\rm l}$ and $M_{\rm r}$. These dependencies are more complicated than those assumed in Sect. 3 as we now have two different upwind Mach numbers. The simple dependencies of Sect. 3 should, however, be recovered in the limit $M_{\rm l} \rightarrow M_{\rm r}$.

The basic physical reason for the more complicated dependencies on the upwind Mach numbers lies in the strong back coupling between the turbulence within the CDL and the driving of this turbulence by the upwind flows. Our asymmetric simulations demonstrate clearly (much more clearly than the symmetric simulations) that the turbulence crucially affects the driving: although $M_{\rm l}$ and $M_{\rm r}$ are strongly different, the corresponding driving efficiencies are about equal, $f_{\rm eff,l} \approx f_{\rm eff,r}$. Thus the efficiency does not primarily depend on the upwind flow. In fact, Fig. 14 shows that for both symmetric and asymmetric runs $f_{\rm eff}$ (averaged now over both shocks) can be well described by

$$f_{\rm eff} = 1 - M_{\rm rms}^{-0.6}. \quad (43)$$

The angle distribution of the two shocks behaves accordingly in that it is similar for both shocks and determined by $M_{\rm rms}$ rather than by either $M_{\rm l}$ or $M_{\rm r}$.

A more detailed analysis of the asymmetric case, including an approximate analytical solution, we are going to present in a subsequent paper.

4.5. Grid and domain studies

The numerical results presented in Sect. 4.2 were all based on simulations with a domain $\mathrm{Y} = 4\mathrm{Y}_0$ and a discretization of $1.5 \cdot 10^{-3}\mathrm{Y}_0$ (R=2) or 2560 cells in y-direction. Here we want to check whether these choices have any systematical effect on the numerical results of Sect. 4.2.

4.5.1. Different y-extent

To check whether the size of the computational domain has any systematic effect on the results of Sect. 4.2, we performed some of the simulations again, but this time on

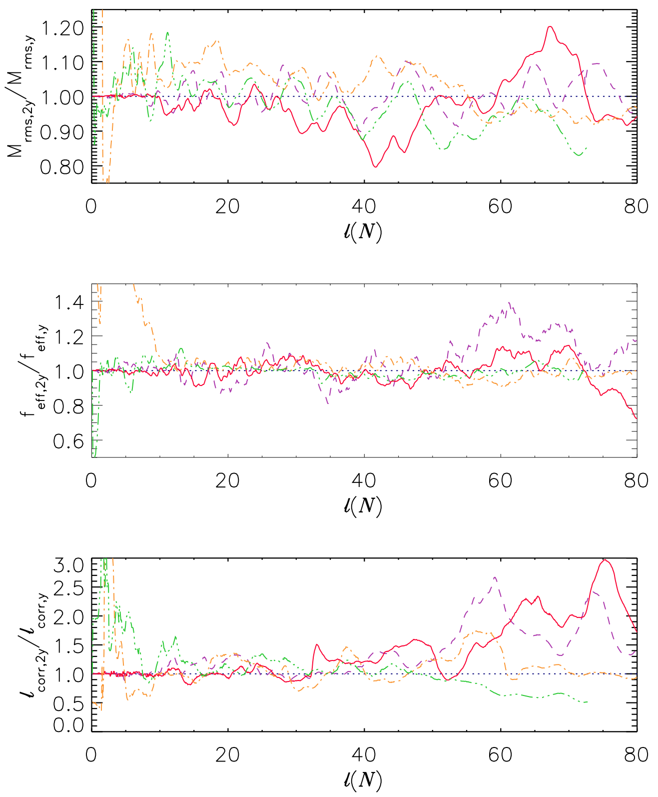

Fig. 15. Comparing runs that differ only in the y-extent of the domain ($\mathrm{Y} = 2\mathrm{Y}_0$ and $\mathrm{Y} = 4\mathrm{Y}_0$). Shown are $M_{\mathrm{rms,2Y}}/M_{\mathrm{rms,Y}}$ (**top**), $f_{\mathrm{eff,2Y}}/f_{\mathrm{eff,Y}}$ (**middle**), and $\ell_{\mathrm{corr,2Y}}/\ell_{\mathrm{corr,Y}}$ (**bottom**). Individual curves denote runs R11_0.2.* (dashed, purple), R22_0.2.* (solid, red), R33_0.2.* (dash-dotted, orange), R43_0.2.* (dash-three-dots, green).

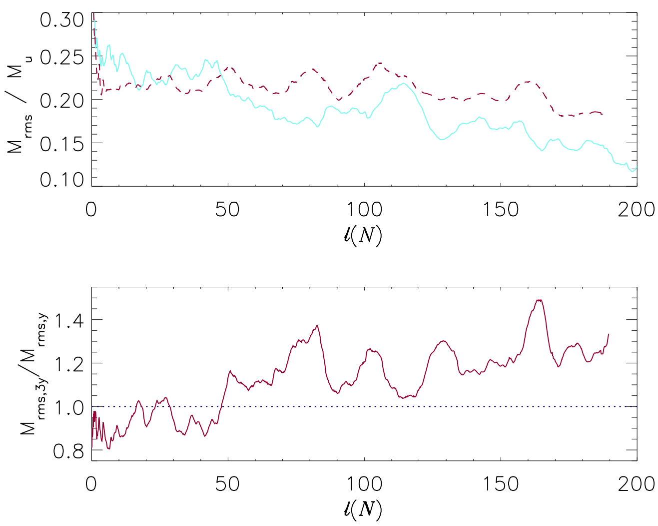

Fig. 16. Comparison of runs R22_0.2.2 and R22_0.2.6, illustrating the effect of a three times larger y-extent of the computational domain on long time scales. Shown are $M_{\mathrm{rms}}/M_{\mathrm{u}}$ (**top**) for R22_0.2.2 (solid, light blue) and R22_0.2.6 (dashed, dark red), and the ratio $M_{\mathrm{rms,3Y}}/M_{\mathrm{rms,Y}}$ (**bottom**).

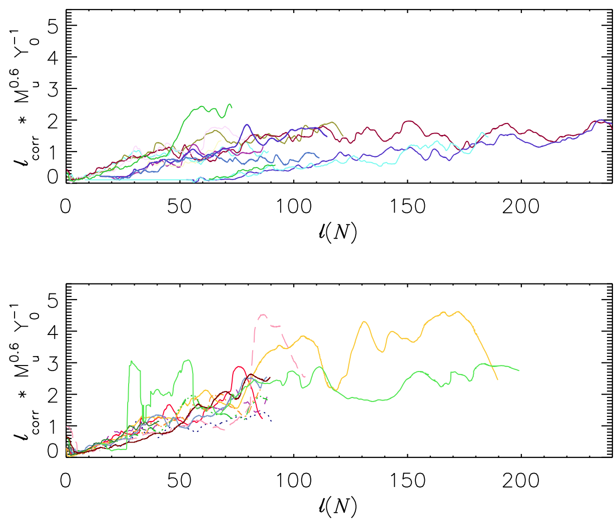

Fig. 17. Scaled auto-correlation lengths of all symmetric simulations on domains with y-extent less or equal to $2\mathrm{Y}_0$ (**top**), and y-extent greater or equal to $4\mathrm{Y}_0$ (**bottom**).

smaller domains of $\mathrm{Y} = 2\mathrm{Y}_0$ and $\mathrm{Y} = \mathrm{Y}_0$. One simulation we performed also on a larger domain $\mathrm{Y} = 6\mathrm{Y}_0$.

Fig. 15 illustrates our findings for simulations on domains $\mathrm{Y} = 2\mathrm{Y}_0$ and $\mathrm{Y} = 4\mathrm{Y}_0$. M_{rms} shows no systematic effect and is, as such, representative for other volume related quantities (Fig. 15, top panel). f_{eff}, as a typical representative for interface related quantities, also shows no clear overall effect of the domain size (Fig. 15, middle panel). The quantity for which we find the most clear effect is the auto-correlation length ℓ_{corr} (Fig. 15, bottom panel). However, even for ℓ_{corr} the effect sets in only for two of the four runs and only for $\ell(N) \gtrsim 30$, i.e. once the CDL extension reaches about half the size of the smaller domain.

For the numerical results in Sect. 4.2 $\ell_{\mathrm{cdl}} \approx \mathrm{Y}/2$ corresponds to $\ell(N) = 60$. We conclude that the y-extent of the computational domain has no apparent systematic effect on these results up to $\ell(N) \lesssim 30$ and likely even up to $\ell(N) \lesssim 60$.

A systematic effect of the computational domain on the numerical solution does become apparent if the simulations are carried on much longer. One pair of runs, R22_0.2.2 and R22_0.2.6, we have carried on much longer, till $\ell(N) \approx 200$. For this pair of runs, Fig. 16 shows the evolution of M_{rms} for each run, as well as their ratio, $M_{\mathrm{rms,3y}}/M_{\mathrm{rms,y}}$. The run on the smaller domain apparently shows after $\ell(N) \approx 100$ a faster decay of M_{rms}. From Fig. 17 we take that the behavior of this one pair of runs is most likely the rule, and not the exception. Fig. 17, top panel, shows ℓ_{corr}, scaled, for all the symmetric runs we have performed and whose domain has a y-extent $\leq 2\mathrm{Y}_0$. Fig. 17, bottom panel, gives the same quantity for all the runs with a domain extention $\geq 4\mathrm{Y}_0$. Comparison of the two figures shows that runs on a domain $\leq 2\mathrm{Y}_0$ saturate around $\ell_{\mathrm{corr}} M_{\mathrm{u}}^{0.6} \approx 1.6\mathrm{Y}_0$. For runs on a domain $\geq 4\mathrm{Y}_0$, ℓ_{corr} reaches much larger values.

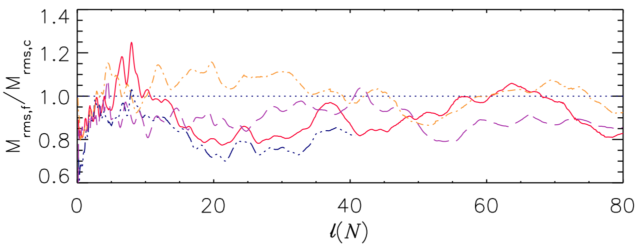

Fig. 18. Comparison of $M_{\rm rms}$ for runs whose spatial resolution differs by a factor of 2 (subscript c = coarse, f = fine). Shown are (giving only the name of the finer run) runs R22_0.2.4 (solid, red), R22_0.4.4 (dash-three-dots, blue), R43_0.2.4 (long dashes, purple), and R11_0.2.4 (dash-dotted, orange).

4.5.2. Different discretization

The results presented in Sect. 4.2 were all based on simulations with a discretization of $1.5 \cdot 10^{-3} Y_0$ (R=2) or 2560 cells in y-direction. To check the effect of the discretization on our results we have repeated several simulations with coarser and/or finer discretization. These simulations reveal indeed a systematic effect of the discretization on the values of average quantities. Nevertheless, the general properties of the solution, its approximate self-similarity and Mach number dependences, remain unaltered. Only the numerical constants $\eta_{\rm i}$ are affected. The changes are, however, small when compared to the differences between the 1D and 2D solution (for example, $\rho_{\rm m} = \eta_1 \rho_{\rm u}$ in 2D while $\rho_{\rm m} = M_{\rm u}^2 \rho_{\rm u}$ in 1D).

We find that finer discretization generally leads to reduced turbulence. Using finer meshes we obtain larger mean densities and smaller values of $M_{\rm rms}$, as shown in Fig. 18. The driving efficiency gets smaller and the shocks become less inclined with respect to the upstream flows, the angle distribution is shifted to smaller values. The characteristic length scale $\ell_{e_{\rm kin}}$ remains about constant if taken units of $\ell_{\rm cdl}$.

A possible explanation for the reduction of turbulence (smaller $M_{\rm rms}$) on finer grids could be the dominance of shocks for the energy dissipation in the CDL. On a coarser grid, the network of shocks within the CDL is less dense. The divergence plots shown in Fig. 19 illustrate this effect. A closer analysis of this idea is, however, beyond the scope of the present paper.

We stress that so far no convergence is reached in our discretization studies. Looking at the comparison of the three runs R22_0.1.4, R22_0.2.4, and R22_0.4.4 in Fig.18 shows that each reduction of the cell size by a factor of two leads to a reduction of about 20% in $M_{\rm rms}$. This indicates that the resolution of 2560 cells in y-direction in our standard runs (R*_0.2.4) and of 5120 cells in y-direction in the refined runs is still not sufficient. This should be kept in mind when interpreting the presented results or any results on shock bound turbulent structures in 2D, let alone 3D.

Also no clear picture emerges with regard to the deviation of $M_{\rm rms}$ from the constant value predicted by Eq. 15.

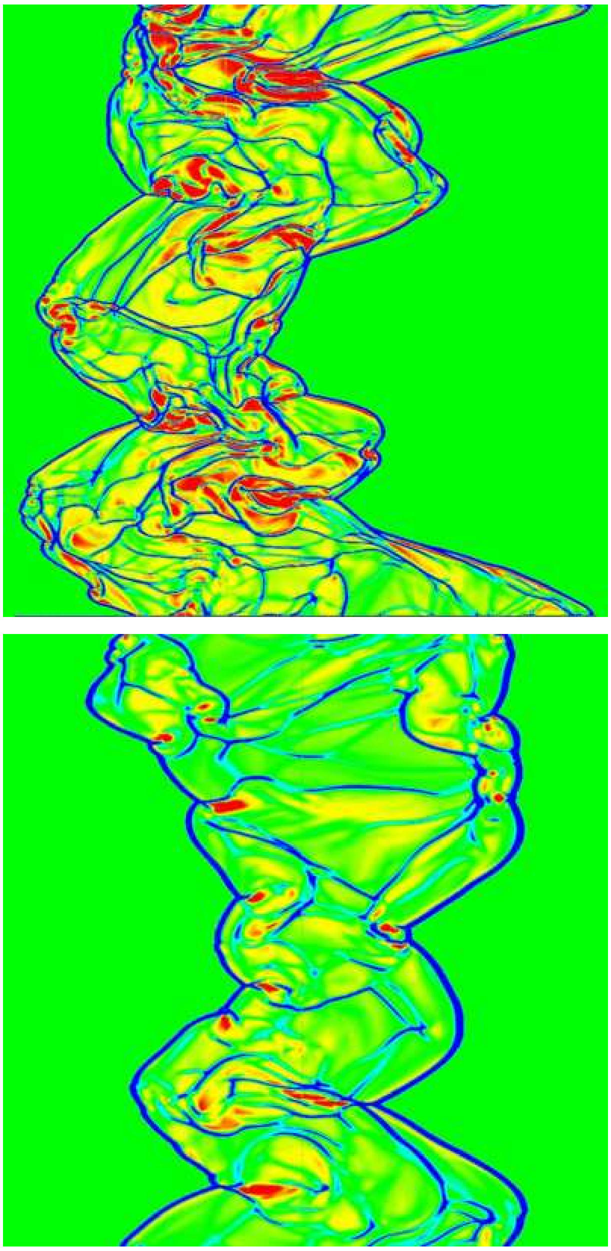

Fig. 19. Plots of div($\boldsymbol{v}$) for two runs that are identical with run R11_0.2.4, shown in Fig. 11, except for their discretization. The runs shown here were computed with two times less (top) and at four times less (bottom) resolution. Blue (dark lines) indicates convergence, red (dark patches) divergence. As can be seen, the number of convergent regions within an average CDL column decreases with decreasing resolution.

A linear fit to $M_{\rm rms}$ for $10 \le \ell(N) \le 70$ yields -12% for run R22_0.2.4 and -23% for the two times coarser run R22_0.1.4. For runs R43_0.*.4 the grid dependence is the other way round: R43_0.2.4 shows a decrease of -25%, the two times coarser run R43_0.1.4 decreases by only -15%.

5. Discussion

We want to address four points in this section. First, we sketch possible reasons for the slight difference between the numerical solution and the relations we derived in Sect. 3. Second, we look once more at the driving of the turbulence and, in particular, the back-coupling between interface and volume properties. Third, we briefly consider our results in an astrophysical context, in particular with regard to molecular clouds. Finally, based on preliminary numerical results, we sketch the effect of some additional physics.

5.1. Numerical solution versus analytical solution

In Sect. 3.2 we suggested that a self-similar solution to our 2D model problem may still exist for the limiting case where the system approaches infinity. The relations derived in that section give a reasonable estimate for the numerical results of Sect. 4. However, while $M_{\rm rms}$ is constant in Sect. 3.2, the numerical simulations show a gradual decrease of $M_{\rm rms}$ already for small CDLs, $\ell_{\rm cdl} \lesssim \mathrm{Y}/2$ (15% decrease of $M_{\rm rms}$ as $\ell(N)$ increases from 10 to 70, Sect. 4.2). We have no firm explanation for this difference. We sketch three possible effects in the following, but stress that the available data do not allow to clearly distinguish between them.

A first, obvious, reason could be the finite y-extent of the computational domain, Y. It sets an upper limit on the total energy input into the CDL, thus on the amount of mass within the CDL that can be driven. Once the CDL becomes has accumulated too much mass the driving per unit mass weakens, the turbulence starts to weaken. The spatial growth of the CDL slows down while the average density increases. The following considerations on time scales may further illustrate the point.

An upper limit for the time at which Y starts to affect the solution is given by the time $t_{\rm y}$ at which $\ell_{\rm cdl} = \mathrm{Y}$. At later times structures may still grow in x-direction (up to $\ell_{\rm cdl}$ at most) but cannot grow any more in y-direction (where Y sets an upper limit). For the runs in Sect. 4.2, $\ell_{\rm cdl} = \mathrm{Y}$ corresponds to $\ell(N) \approx 120$ or $t_{\rm y} = 12\mathrm{Y}_0/v_{\rm rms}$. A lower limit for the decay time scale of the turbulence may be obtained as follows. For the case of uniformly driven isothermal hydrodynamic turbulence in a 3D periodic box, Mac Low (1999) has shown that the typical decay time once the driving is turned off, t_0, and the initial driving wave-length, $\lambda_{\rm drv}$, are related by $t_0 \approx \lambda_{\rm drv}/v_{\rm rms}$. Assuming that this result holds also for our slab, that $\lambda_{\rm drv} = \mathrm{Y}$, and that driving is turned off completely, it follows that $t_0 \approx \mathrm{Y}/v_{\rm rms}$, or $t_0 \approx 4\mathrm{Y}_0/v_{\rm rms}$ for the runs in Sect. 4.2. However, driving continues in our simulations and so the effective decay time scale of the turbulence is likely much longer than t_0. Finally, for the runs in Sect. 4.2, a typical integration time of $\ell(N) = 60$ corresponds to about $\tau = 6\mathrm{Y}_0/v_{\rm rms}$, a typical turbulent crossing time at $\ell(N) = 60)$ is $\tau_{\rm cross} = \ell_{\rm cdl}/v_{\rm rms} \approx 2\mathrm{Y}_0/v_{\rm rms}$. Comparing these different time scales it seems likely that at $\ell(N) = 60$, turbulence in the center of the CDL is still essentially driven, not essentially decaying.

Our simulation data do not allow to either clearly confirm or reject the hypothesis that the finite y-extent of the computational domain is responsible for the slight decrease of $M_{\rm rms}$ which we observe at early times, $\ell(N) \lesssim 70$. If the finite domain size were responsible, $M_{\rm rms}$ should decay differently on different domains. Comparison of simulations on different domains up to $\ell(N) \approx 70$ (Sect. 4.5.1) gives, however, no clear picture. The data are rather noisy and simulations on domains $2\mathrm{Y}_0$ and $4\mathrm{Y}_0$ show no systematic differences as long as $\ell(N) \lesssim 30$ ($\ell_{\rm cdl} < \mathrm{Y}/2$ on the smaller domain). Only for much later times, $\ell(N) >> 70$, well beyond the range for the results in Sect. 4.2, Y has a clear effect and $M_{\rm rms}$ decreases faster on smaller domains (Fig. 16).

A second, more speculative, reason might be numerical dissipation, provided that its effect were to increase with $\ell_{\rm cdl}$. While we have no evidence that the latter is really the case, it may also be hasty to discard this possibility right away. Porter & Woodward (1994) found, by observing how simple 2D hydrodynamical flows (shear flows and sound waves of definite wave number, their section 3.3) damp with time, that the decay rate due to numerical dissipation alone is a non-linear function of the wave number. Their results are certainly not directly applicable to the present case. But in view of these results, and given the change of structure size with $\ell_{\rm cdl}$ as suggested by Fig. 3, it might be possible that the effect of numerical dissipation indeed changes with $\ell_{\rm cdl}$. Note that this would also imply that the MILES approach, outlined in Sect. 2.1, were not strictly valid for the problem we consider. The currently available data do not allow us to clearly reject or confirm the effect.

A third reason, or rather an amplifying mechanism, could be back-coupling between $M_{\rm rms}$ and the driving efficiency. Once the turbulence within the CDL is slightly reduced (for whatever reason), the reduction is further amplified by the back-coupling between turbulence and driving, $f_{\rm eff} = (1 - M_{\rm rms}^{-0.6})$. The decrease of $M_{\rm rms}$ results in smaller inclination of the shocks with respect to the upstream flows, more energy is dissipated at the confining shocks of the CDL, and less driving energy enters the CDL. For the observed 15% reduction of $M_{\rm rms}$, the reduced driving may, in fact, play a dominant role: as $\ell(N)$ increases from 10 to 70, $\dot{\mathcal{E}}_{\rm drv}/\dot{\mathcal{E}}_{\rm drv}^{\rm th}$ decreases by 13% (Sect. 4.2.3). But to really estimate the relative importance of the three effects just sketched, further studies are certainly necessary.

Two more points seem noteworthy to us in this section. One concerns the near independence of $\dot{\mathcal{E}}_{\rm diss}$ on $\ell_{\rm cdl}$. From Fig. 3 (increase in structure size with increasing $\ell_{\rm cdl}$) we take that it is rather the increasing average distance between shocks that allows $\dot{\mathcal{E}}_{\rm diss}$ to be essentially independent of $\ell_{\rm cdl}$, and not so much the, on average, decreasing strength of shocks (Sect. 3.2.3). Whether this is indeed true, only a closer analysis of the structure within the CDL along the lines of Mac Low & Ossenkopf (2000) can tell which is, however, beyond the scope of the present paper. Such an analysis could also shed light on whether (or in which sense) $\ell_{\rm e_{kin}}$ (see Sect. 4.2.3) is indeed a measure for the average distance between shocks. It would also allow to quantify our impression that small scale structures are preferably located close to the confining interfaces. If true, this would fit with the result by Smith et al. (2000) that the high frequency part of the shock spectrum is lost most efficiently.

The other point concerns run R5_0.2.4. With $\mathrm{corr}(\rho, v) \approx -0.4$ $M_{\mathrm{rms}} \approx 0.9$ it violates two of the basic assumptions we made in Sect. 3.2. Its mean density is close to the isothermal value for strong shocks, $\rho_{\mathrm{m}} \approx 22\rho_{\mathrm{u}} \approx 0.9\rho_{\mathrm{u}} M_{\mathrm{u}}^2$. Both $\dot{\mathcal{E}}_{\mathrm{diss}}$ and $\dot{\mathcal{E}}_{\mathrm{drv}}$ increase with ℓ_{cdl}. With these characteristics, R5_0.2.4 may mark the transition from compressible supersonic turbulence, the topic of this paper, to compressible subsonic turbulence.

5.2. CDL and confining shocks: a coupled system

The turbulence within the CDL is 'naturally driven' in the sense that we control neither what fraction of the total upstream kinetic energy, $\rho_{\mathrm{u}} M_{\mathrm{u}}^2$, really enters the CDL nor the spatial scale on which this energy input varies. Both are directly determined by the confining shocks instead, and indirectly depend on the system as a whole. The driving efficiency at each confining shock scales with M_{rms}, even for situations where $M_{\mathrm{l}} \neq M_{\mathrm{r}}$ (see Sect. 4.4). The auto-correlation length of the confining shocks and the characteristic length scale of the turbulence within the CDL are proportional to each other, both scaling as $\ell_{\mathrm{cdl}} M_{\mathrm{u}}^{-0.6}$. We take these facts as evidence that the CDL as a whole, its interface and volume properties, forms a tightly coupled, quasi-stationary and self-regulating system. Back coupling between post shock flow and shock is also described in other contexts, for example by Foglizzo (2002) for the case of Bondi-Hoyle accretion.

An aspect that remained elusive in Sect. 4 is the spatial scale on which the energy input varies, the energy injection scale. To really tackle this issue it would be necessary to analyze the energy spectrum of the CDL. This task requires, however, some caution because of the highly irregular boundary of the CDL, and we postpone it for the moment. Nevertheless, we would like to present a few thoughts on the subject.

A first question is whether it is justified to speak at all of only one injection scale, of monochromatic driving. The homogeneous upstream flow is modulated by the confining shocks. These are wiggled on a variety of spatial scales at any given moment. This strongly suggests that the kinetic energy input into the CDL is most likely not monochromatic but occurs at a whole spectral range instead. Consequences of such non-monochromatic driving have been studied, for example, by Norman & Ferrara (1996).

It also seems worthwhile to briefly look at monochromatically driven turbulence, in particular at the numerical simulations by Mac Low (1999). For the case of artificially, monochromatically driven hydrodynamic turbulence in a 3D box with periodic boundaries, he found that the characteristic length of the turbulence is proportional to the driving wave length, independent of the Mach number: $\lambda/\ell^{3\mathrm{d}}_{\mathrm{e_{kin}}} = 1.42$, where λ is the (known) driving wave-length and $\ell^{3\mathrm{d}}_{\mathrm{e_{kin}}}$ is the 3D analogon of $\ell_{\mathrm{e_{kin}}}$ in Eq. 41. In addition, Mac Low (1999) observed that $\ell^{3\mathrm{d}}_{\mathrm{e_{kin}}}$ increases with λ, which is mirrored in the apparent increase of the structure size (patches, filaments).

Although our setting clearly differs from that of Mac Low (1999), two thoughts come to mind. The first is an observation actually, namely that we also observe an increase in structure size with $\ell_{\mathrm{e_{kin}}}$. The second thought is more of a question or speculation. Mac Low (1999) determines the proportionality constant between the characteristic scale of the turbulence and the monochromatic driving wave-length. One may wonder about the implications of this finding if not one driving wave-length is present but a whole spectrum. How will the characteristic length scale of the turbulence, which can still be determined following Eq. 41, depend on this spectrum? And, given our finding that $\ell_{\mathrm{e_{kin}}} \propto \ell_{\mathrm{corr}}$, what does ℓ_{corr} tell us about this spectrum? Both questions should become tractable once the energy spectrum of the CDL is determined.

5.3. A glimpse at astrophysics

With regard to astrophysics, the presented work basically suggests that, within the frame of isothermal hydrodynamics and a roughly plane parallel setting, larger Mach numbers of the colliding flows results in a finer and finer network of higher and higher density contrast within the interaction zone. In different types of wind-driven structures this connection between Mach number and structure may be directly observable.

For the clumping of line-driven hot star winds, our results suggest that the sheets or clumps formed by the instability of the line-driving are not homogeneous but possess fine-scale substructure with large density contrast.

Concerning molecular clouds we first mention that recent arguments support the idea, originally brought forward by Hunter (1979) and Larson (1981), that molecular clouds result from the collision of large scale flows in the ISM. Basu & Murali (2001) make the point that small scale driving ($\approx$ 0.1 - 1 pc) of molecular clouds is incompatible with observed total luminosities, unless the energy dissipation rates derived from MHD simulations are seriously overestimated. Using a principal component analysis of ^{12}CO (J=1-0) emission, Brunt (2003) identify large-scale flows of atomic material in which the globally turbulent molecular clouds are embedded. Similar observational results were reported by Ballesteros-Paredes et al. (1999a).

Driven supersonic turbulence as a structuring agent for the interior of molecular clouds was examined by many authors (Hunter et al. 1986; Elmegreen 1993; Vazquez-Semadent et al. 1995; Mac Low et al. 1998; Ballesteros-Paredes et al. 1999a,b; Mac Low 1999; Hartmann et al. 2001; Joung & Mac Low 2004; Burkert & Hartmann 2004;

Mac Low & Klessen 2004; Audit & Hennebelle 2005; Heitsch et al. 2005; Kim & Ryu 2005; Vázquez-Semadeni et al. 2006; Ballesteros-Paredes et al. 2006). The driving wave-length of the turbulence, and thus the largest structure size (Mac Low 1999; Ballesteros-Paredes & Mac Low 2002), is usually a free parameter. Our results show instead that at least for the case of an isothermal, shock compressed, supersonically turbulent 2D slab, the structure size rather depends on the size of the slab or cloud.

5.4. Additional physics: an outlook

The model presented in this paper covers only some very basic physics. To obtain results with a more direct relation to reality, additional physics must be included in the future, among these the following. Strongly asymmetric flows, where $M_\mathrm{l} \neq M_\mathrm{r}$, lead to more complicated dependences, as we will demonstrate in a forthcoming paper. Inclusion of radiative cooling, instead of assuming isothermal conditions, can affect the problem in different ways. Thermal instability can lead to additional dynamical effects (Chevalier & Imamura 1982; Gaetz et al. 1988; Strickland & Blondin 1995; Walder & Folini 1996b; Hennebelle & Pérault 1999, 2000; Vázquez-Semadeni et al. 2000; Koyama & Inutsuka 2002; Audit & Hennebelle 2005; Heitsch et al. 2005; Pittard et al. 2005; Mignone 2005). Extended cooling layers, on the other hand, tend to act as a cushion. Simulations by Walder & Folini (1999) and Walder & Folini (2000b), which include radiative cooling but have otherwise similar parameters as some of the simulations presented here, show comparatively more small scale structure and even roll-ups at the interfaces confining the CDL. The CDL as a whole evolves less violently and mean densities are about a factor of four to eight larger that what we found here for the isothermal case. Strongly asymmetric flows, where $M_\mathrm{l} \neq M_\mathrm{r}$, lead to a qualitatively different solution if radiative cooling is included (Walder & Folini 1998b), and to more complicated dependences on the upwind Mach numbers in the isothermal case, as we will demonstrate in a forthcoming paper. The role of thermal conduction is only considered by relatively few publications so far (Begelman & McKee 1990; Myasnikov & Zhekov 1998; Koyama & Inutsuka 2004). Global bending of the interaction zone affects the stability properties of the interaction zone as a whole and thus probably also its interior properties. In colliding wind binaries for example, matter is transported out of the central part of the system and diluted in the outer part. Simulations of bow shocks and colliding winds in binaries show strong traveling waves, together with a systematic change of the mean properties in the flow off from the stagnation point (Stevens et al. 1992; Walder & Folini 1995; Blondin & Koerwer 1998).

6. Summary and Conclusions

We looked at symmetric, supersonic ($5 \lesssim M_\mathrm{u} \lesssim 90$), isothermal, plane parallel colliding flows in 2D. The resulting shock confined interaction zone (CDL) is supersonically turbulent ($1 \lesssim M_\mathrm{rms} \lesssim 10$). We investigated the CDL, and its interplay with the upstream flows, by dimensional analysis and numerical simulations. The latter we generally stopped when $\ell_\mathrm{cdl} \approx \mathrm{Y}/2$. The results are interesting not only with regard to flow collisions but also shed new light on the properties of supersonic turbulence in general.

The numerical simulations show that the CDL has an irregular shape, and a patchy, supersonically turbulent interior. The driving of the turbulence is natural in that it depends on the shape of the confining shocks.

The dimensional analysis is based on isothermal Euler equations in infinite space. Within this frame, a self-similar solution may exist, which would depend on M_u but must not depend on ℓ_cdl. Under some further, simplifying assumptions relations for average quantities are obtained (Sect.3.3).

Based on both, the analytical and numerical result, we arrive at the following conclusions.

1) Comparison of the numerical and the self-similar solution shows generally good agreement if $M_\mathrm{rms} \gtrsim 1$. The modest deviation between the numerical and the self-similar solution increases with ℓ_cdl. We suggest some explanations for the deviation, but our data do not allow any clear conclusions on the issue. For $M_\mathrm{rms} \lesssim 1$ we have but one simulation. It shows clear differences to the other runs and may be more characteristic for compressible subsonic turbulence than for supersonic turbulence.

2) The CDL is characterized by $M_\mathrm{rms} \approx \eta_1^{-1/2} M_\mathrm{u}$ and $\rho_\mathrm{m} \approx \eta_1 \rho_\mathrm{u}$. The average compression ratio of the CDL thus is independent of M_u. This is in sharp contrast to the 1D case, where $\rho_\mathrm{m,1d} = M_\mathrm{u}^2 \rho_\mathrm{u}$. From the numerical simulations we find $\eta_1 \approx 30$.

3) The turbulence within the CDL and the driving efficiency are related by $f_\mathrm{eff} = 1 - M_\mathrm{rms}^{-0.6}$. The relation also holds for asymmetric settings, where $M_\mathrm{l} \neq M_\mathrm{r}$, emphasizing the mutual coupling between volume and interface properties. For larger upstream Mach numbers, the shocks confining the interaction zone are more strongly inclined with respect to the upstream flows. The driving is more efficient, a larger fraction of the upstream kinetic energy is dissipated only within the CDL and not already at the confining shocks.

4) The characteristic length scale of the turbulence, ℓ_{e_kin}, and the auto-correlation length of the confining shocks, ℓ_corr, are proportional to each other. Both scale as $\ell_\mathrm{cdl} M_\mathrm{u}^{-0.6}$. This although the former is based on volume quantities while the later is derived from interface properties.

5) The separation of filaments and the size of patches within the CDL both get larger as ℓ_cdl increases and/or M_u decreases.

For increasing upstream Mach numbers we thus expect, in summary, a faster expanding CDL with more strongly inclined confining interfaces with respect to the upstream flows, similar mean density, finer interior structure relative to the CDL size, and a gradual shift of the energy dissipation from the confining shocks to internal shocks within the CDL. We expect to observe these general dependencies in real objects where shock confined slabs play a role, like molecular clouds, wind driven structures, supernova remnants, or γ-ray burst.

Acknowledgements. The authors wish to thank the crew running the Cray SV1 at ETH Zürich, where the simulations were performed, the system administrator of institute for astronomy, ETH Zürich, P. Steiner, for steady support, and J. Favre from the Swiss Center of Scientific Computing CSCS/SCSC, Manno, for graphics support. The authors also would like to thank the referee, E. Vazquez-Semadeni, for the detailed and engaged report.

References

Anninos, P. & Norman, M. L. 1996, ApJ, 460, 556
Audit, E. & Hennebelle, P. 2005, A&A, 433, 1
Ballesteros-Paredes, J., Gazol, A., Kim, J., Klessen, R. S., Jappsen, A.-K., & Tejero, E. 2006, ApJ, 637, 384
Ballesteros-Paredes, J., Hartmann, L., & Vazquez-Semadeni, E. 1999a, ApJ, 527, 285
Ballesteros-Paredes, J. & Mac Low, M. 2002, ApJ, 570, 734
Ballesteros-Paredes, J., Vázquez-Semadeni, E., & Scalo, J. 1999b, ApJ, 515, 286
Basu, S. & Murali, C. 2001, ApJ, 551, 743
Begelman, M. C. & McKee, C. F. 1990, ApJ, 358, 375
Berger, M. J. 1985, Lectures in applied Mathematics, 22, 31
Blondin, J. M. & Koerwer, J. F. 1998, New Astronomy, 3, 571
Blondin, J. M. & Marks, B. S. 1996, New Astronomy, 1, 235
Boris, J., Grinstein, F., Oran, E., & Kolbe, R. 1992, Fluid. Dynam. Res, 10, 199
Brunt, C. M. 2003, ApJ, 280
Burkert, A. & Hartmann, L. 2004, ApJ, 616, 288
Chevalier, R. A. & Imamura, J. N. 1982, ApJ, 261, 543
Colella, P. 1990, Journal of Computional Physics, 87, 171
Colella, P. & Woodward, P. R. 1984, Journal of Computational Physics, 54, 174
Corcoran, M. F., Pittard, J. M., Stevens, I. R., Henley, D. B., & Pollock, A. M. T. 2005, in X-Ray and Radio Connections (eds. L.O. Sjouwerman and K.K Dyer) Published electronically by NRAO, http://www.aoc.nrao.edu/events/xraydio Held 3-6 February 2004 in Santa Fe, New Mexico, USA, (E2.02) 13 pages
Elmegreen, B. G. 1993, ApJ, 419, L29+
Elmegreen, B. G. & Scalo, J. 2004, Ann. Rev. of Astronomy & Astrophysics, 42, 211
Fan, Y. Z. & Wei, D. M. 2004, ApJ, 615, L69
Feldmeier, A. & Owocki, S. 1998, Ap&SS, 260, 113
Feldmeier, A., Puls, J., & Pauldrach, A. W. A. 1997, A&A, 322, 878
Foglizzo, T. 2002, A&A, 392, 353
Folini, D. & Walder, R. 2000, in ASP Conf. Ser. 204: Thermal and Ionization Aspects of Flows from Hot Stars, 267–280
Gaetz, T. J., Edgar, R. J., & Chevalier, R. A. 1988, ApJ, 329, 927
Gammie, C. F. & Ostriker, E. C. 1996, ApJ, 466, 814
Garnier, E., Mossi, M., Sagaut, P., Comte, P., & Deville, M. 1999, Journal of Computational Physics, 153, 273
Ghisellini, G., Celotti, A., & Costamante, L. 2002, A&A, 386, 833
Hartmann, L., Ballesteros-Paredes, J., & Bergin, E. A. 2001, ApJ, 562, 852
Heitsch, F., Burkert, A., Hartmann, L. W., Slyz, A. D., & Devriendt, J. E. G. 2005, ApJ, 633, L113
Hennebelle, P. & Pérault, M. 1999, A&A, 351, 309

—. 2000, A&A, 359, 1124
Heyer, M. H. & Brunt, C. M. 2004, ApJ, 615, L45
Hirsch, C. 1995, Numerical computation of internal and external flows, Vol. 1, Fundamentals of discretization (John Wiley and Sons)
Hueckstaedt, R. M. 2003, New Astronomy, 8, 295
Hunter, J. H. 1979, ApJ, 233, 946
Hunter, J. H., Sandford, M. T., Whitaker, R. W., & Klein, R. I. 1986, ApJ, 305, 309
Jasak, H. & Weller, H. 1995, internal Report, CFD research group, Imperial College, London
Joung, M. K. R. & Mac Low, M.-M. 2004, American Astronomical Society Meeting Abstracts, 204,
Kaiser, C. R., Sunyaev, R., & Spruit, H. C. 2000, A&A, 356, 975
Kang, H., Ryu, D., Cen, R., & Song, D. 2005, ApJ, 620, 21
Kim, J. & Ryu, D. 2005, ApJ, 630, L45
Klein, R. I., Woods, D. T., & Tod, D. 1998, ApJ, 497, 777
Koyama, H. & Inutsuka, S.-i. 2002, ApJ, 564, L97
—. 2004, ApJ, 602, L25
Larson, R. B. 1981, MNRAS, 194, 809
Lele, S. 1992, Journal of Computional Physics, 103, 16
Lesieur, M. 1999, Turbulence in fluids (fluid mechanics and its applications) (Springer)
LeVeque, R. 2002, Finite volume methods for hyperbolic problems (Cambridge University Press)
Mac Low, M. . & Ossenkopf, V. 2000, A&A, 353, 339
Mac Low, M. & Klessen, R. S. 2004, Reviews of Modern Physics, 76, 125
Mac Low, M.-M. 1999, ApJ, 524, 169
Mac Low, M.-M., Klessen, R., & Burkert, A. 1998, Phys. Rev. Letters, 80(3), 2754
Marchenko, S. V., Moffat, A. F. J., Ballereau, D., Chauville, J., Zorec, J., Hill, G. M., Annuk, K., Corral, L. J., Demers, H., Eenens, P. R. J., Panov, K. P., Seggewiss, W., Thomson, J. R., & Villar-Sbaffi, A. 2003, ApJ, 596, 1295
Matzner, C. D. & McKee, C. F. 1999, ApJ, 526, L109
Mignone, A. 2005, ApJ, 626, 373
Mimica, P., Aloy, M. A., Müller, E., & Brinkmann, W. 2004, A&A, 418, 947
Myasnikov, A. V. & Zhekov, S. A. 1998, MNRAS, 300, 686
Norman, C. A. & Ferrara, A. 1996, ApJ, 467, 280
Nussbaumer, H. & Walder, R. 1993, A&A, 278, 209
Oskinova, L. M., Feldmeier, A., & Hamann, W.-R. 2004, A&A, 422, 675
Owocki, S. P., Castor, J. I., & Rybicki, G. B. 1988, ApJ, 335, 914
Panaitescu, A., Spada, M., & Mészáros, P. 1999, ApJ, 522, L105
Piran, T. 2004, Reviews of Modern Physics, 76, 1143
Pittard, J. M., Dobson, M. S., Durisen, R. H., Dyson, J. E., Hartquist, T. W., & O'Brien, J. T. 2005, A&A, 438, 11
Porter, D., Pouquet, A., & Woodward, P. 1992, Theor. Comput. Fluid Dyn., 4, 13
—. 1994, Phys. Fluids, 6, 2133
Porter, D. H. & Woodward, P. R. 1994, ApJ Supp., 93, 309
Quirk, J. J. 1994, Internat. J. Numer. Methods Fluids, 18, 555
Rees, M. J. & Meszaros, P. 1994, ApJ, 430, L93
Robinet, J.-C., Gressier, J., Casalis, G., & Moschetta, J.-M. 2000, Journal of Fluid Mechanics, 417, 237
Scalo, J. & Elmegreen, B. G. 2004, Ann. Rev. of Astronomy & Astrophysics, 42, 275
Smith, M. D., Mac Low, M.-M., & Zuev, J. M. 2000, A&A, 356, 287
Stevens, I. R., Blondin, J. M., & Pollock, A. M. T. 1992, ApJ, 386, 265
Strickland, D. & Blondin, J. M. 1995, ApJ, 449, 727
Vázquez-Semadeni, E. 2004, Ap&SS, 292, 187
Vázquez-Semadeni, E., Gazol, A., & Scalo, J. 2000, ApJ, 540, 271
Vázquez-Semadeni, E., Ryu, D., Passot, T., González, R. F., & Gazol, A. 2006, ApJ, 643, 245
Vazquez-Semadent, E., Passot, T., & Pouquet, A. 1995, ApJ, 441, 702
Vishniac, E. T. 1994, ApJ, 428, 186
Walder, R. & Folini, D. 1995, in IAU Symposia, Vol. 163, 525
Walder, R. & Folini, D. 1996a, A&A, 315, 265
—. 1996b, A&A, 315, 265
—. 1998a, A&A, 330, L21
—. 1998b, A&A, 330, L21
Walder, R. & Folini, D. 1999, in Hyperbolic Problems: Theory, Numerics, Applications, ed. M.Fey & R.Jeltsch, 973–982
Walder, R. & Folini, D. 2000a, in Thermal and Ionization Aspects of Flows from Hot Stars: Observations and Theory, ed. H. J. G. L. M. Lamers & A. Sapar, ASP Conference Series, 281–285
—. 2000b, Ap&SS, 274, 343

Appendix A: Numerical computation of obliqueness angle

While shocks are smeared over approximately 3 grid cells in our simulations, the confining shocks in our analysis are specified as a series of discrete x,y-coordinate pairs only (see Sect. 4.2.2). This information is sufficient to compute most shock related quantities to good accuracy, for example the shock length $\ell_{\rm sh}$. The only quantity that requires a more careful proceeding is the obliqueness angle α. If it were computed directly from the discrete shock positions, only discrete values would be obtained, for example 0°, 45°, 63.4° etc. for one-sided differences.

To compute the obliqueness angle $\alpha_{\rm i}(y_{\rm j})$ (see Fig. 1 and Sect. 4.2.2) at each position $y_{\rm j}$, $1 \le j \le J$, of the left and right shock ($s_{\rm l}$ and $s_{\rm r}$), we proceed as follows. In a first step, we use spline interpolation to double the number of points in y-direction along the shock front. Next, we smooth the shock front slightly, using a running mean with an averaging window of ± 5 points (this corresponds to an averaging window of ± 2.5 points in the original data. Then we compute the derivative at each point of this smoothed shock front, using a 3-point Lagrangian interpolation. To avoid abrupt changes in the derivative from one point to the next, we smooth again by a running mean with averaging window ± 5 points. The obliqueness angle $\alpha_{\rm i}(y_{\rm j})$, $1 \leq j \leq 2J$, we finally obtain as the arctan of the derivative.

We have checked that the size of the averaging window (± 3 points or ± 7 points) has only a marginal effect on the angle distribution and the driving efficiency. For the latter, which is an integral over both shocks, test show that α can even be computed directly from the discrete positions.

Appendix B: List of runs, their parameters and their naming schemes

Table B.1. List of performed simulations. Individual columns contain (column number in square brackets): label of run [1], following the scheme label= $\mathrm{M_u}$_I.R.Y, where I is the initial condition, R the refinement factor such that cell size = $3.125 \cdot 10^{-3}\mathrm{Y}_0/\mathrm{R}$, and Y is the y-extension of the computational domain in units of Y_0; Mach number of upstream flow, M_u [2]; stopping time of simulation in terms of $\ell(N)$ [3]; y-averaged x-extension of CDL at stopping time, relative to y-extent of computational domain, $\ell_\mathrm{cdl}/\mathrm{Y}$ [4]; average quantities [5-9] of: rms Mach number, M_rms [5]; mean density in units of upstream density, $\rho_\mathrm{m}/\rho_\mathrm{u}$ [6]; shock length in units of y-domain, ℓ_sh/Y [7]; driving efficiency, f_eff [8]; averages taken over $10 \le \ell(N) \le 70$ for I=0 and over $60 \le \ell(N) \le 120$ for I=1, for I=2 we give the values at the end of the simulation in parentheses instead.

label	M_u	$\ell(N)$	$\ell_\mathrm{cdl}/\mathrm{Y}$	M_rms	$\frac{\rho_\mathrm{m}}{\rho_\mathrm{u}}$	$\frac{\ell_\mathrm{sh}}{Y}$	f_eff
Symmetric runs, no CDL at t=0							
R5_0.2.4	5.42	91	1.07	0.90	24	1.1	0.16
R11_0.2.4	10.85	88	0.59	2.2	33	1.5	0.35
R22_0.2.4	21.7	86	0.30	4.6	30	2.6	0.59
R33_0.2.4	32.4	86	0.50	6.9	26	3.6	0.70
R43_0.2.4	43.4	88	0.55	9.1	29	4.6	0.76
R87_0.2.4	86.8	105	0.82	15.	23	12.1	0.89
R22_0.4.4	21.7	41	0.25	4.3	35	2.3	0.55
R22_0.1.4	21.7	88	0.74	5.0	26	2.7	0.62
R43_0.1.4	43.4	90	0.59	8.9	32	4.1	0.76
R11_0.2.2	21.7	89	1.10	2.2	33	1.4	0.33
R22_0.2.2	21.7	307	0.79	4.7	28	2.6	0.59
R33_0.2.2	32.4	82	1.45	6.7	30	3.6	0.70
R43_0.2.2	43.4	73	1.09	9.4	27	4.7	0.76
R22_0.2.6	21.7	190	0.84	4.7	29	2.6	0.60
Symmetric runs, with CDL at t=0							
R22_1.2.2	21.7	87	0.83	3.3	61	1.9	0.50
R22_1.2.1	21.7	111	1.33	3.2	68	1.8	0.46
R22_1.4.4	21.7	199	0.72	3.4	59	1.9	0.49
R22_1.4.2	21.7	68	0.40	2.8	91	1.6	0.39
R22_1.1.2	21.7	115	1.21	3.9	42	2.4	0.59
R22_2.2.2	21.7	313	1.44	(2.4)	(109)	(1.5)	(0.34)
R22_2.4.2	21.7	186	0.37	(1.8)	(253)	(1.2)	(0.24)
R22_2.8.2	21.7	92	0.14	(1.4)	(281)	(1.2)	(0.21)